NEUROSCIENCE

Synchronous and opponent thermosensors use flexible cross-inhibition to orchestrate thermal homeostasis

Luis Hernandez-Nunez[1,2,3]*, Alicia Chen[1,2,4], Gonzalo Budelli[5,6,7†], Matthew E. Berck[8], Vincent Richter[9], Anna Rist[9], Andreas S. Thum[9], Albert Cardona[8,10,11], Mason Klein[12]*, Paul Garrity[5,6,7]*, Aravinthan D. T. Samuel[1,2]*

Body temperature homeostasis is essential and reliant upon the integration of outputs from multiple classes of cooling- and warming-responsive cells. The computations that integrate these outputs are not understood. Here, we discover a set of warming cells (WCs) and show that the outputs of these WCs combine with previously described cooling cells (CCs) in a cross-inhibition computation to drive thermal homeostasis in larval *Drosophila*. WCs and CCs detect temperature changes using overlapping combinations of ionotropic receptors: Ir68a, Ir93a, and Ir25a for WCs and Ir21a, Ir93a, and Ir25a for CCs. WCs mediate avoidance to warming while cross-inhibiting avoidance to cooling, and CCs mediate avoidance to cooling while cross-inhibiting avoidance to warming. Ambient temperature–dependent regulation of the strength of WC- and CC-mediated cross-inhibition keeps larvae near their homeostatic set point. Using neurophysiology, quantitative behavioral analysis, and connectomics, we demonstrate how flexible integration between warming and cooling pathways can orchestrate homeostatic thermoregulation.

INTRODUCTION

Body temperature affects all physiological processes and thus must be tightly controlled. In mammals, the preoptic area of the hypothalamus functions as a thermostat by combining the outputs of multiple warming- and cooling-activated cells to regulate physiological and behavioral mechanisms that keep body temperature near the homeostatic set point (*1*–*3*). The computations that integrate warming cell (WC) and cooling cell (CC) outputs are not understood. The use of multiple physiological thermoregulatory mechanisms (e.g., evaporation of sweat for cooling and cutaneous vasoconstriction for warming) and behavioral mechanisms (navigation toward regions with warmer or colder ambient temperatures) makes it difficult to isolate the computations underlying thermoregulation in mammals.

Poikilotherms such as reptiles, fish, and insects lack physiological mechanisms to substantially warm or cool their bodies (*4*). These animals rely on behavior to locate regions with ambient temperatures closer to their homeostatic set point. To do this, many poikilotherms, including cave beetles (*5*) and larval *Drosophila* (*6*), have evolved exquisite neural and behavioral thermosensitivities (<0.005°C/s), making them ideal to study the computations underlying thermal homeostasis.

The context in which cooling and warming must be interpreted in the brain is dependent on ambient temperature. When ambient temperature is below the homeostatic set point, cooling should evoke avoidance behaviors. When ambient temperature is above the homeostatic set point, warming should evoke avoidance behavior, and at the homeostatic set point, any avoidance behavior should be inhibited. Thus, the outputs of thermosensory cells must be integrated flexibly to achieve thermoregulation.

Previous studies in *Caenorhabditis elegans* (*7*), larval and adult *Drosophila melanogaster* (*4*), larval zebrafish (*8*), and rodents (*9*) have focused on the physiology of single thermosensory cell types and their contribution to thermoregulation in a specific ambient temperature context. Deriving a computation that incorporates the flexibility needed in different contexts requires determining how an animal integrates the contributions of both cooling- and warming-responsive cells across ambient temperatures.

Here, we investigate the sensory cells and computations that control larval *Drosophila* body temperature. Previous work uncovered three CCs in the dorsal organ ganglion (DOG). The CCs are sensitive to temperature changes at ambient temperatures from 14° to 34°C (the innocuous temperature range). The CCs are required for cooling avoidance from as low as 14°C toward 24°C (the homeostatic set point) but are not required for innocuous warming avoidance above 24°C (*6*). Larval *Drosophila* do not express the adult innocuous warming receptor Gr28b(d) (*10*, *11*) and use the Transient receptor potential cation channel, subfamily A, member 1 (TrpA1) channel to mediate rolling escape responses to noxious heat (*12*). The molecular and cellular sensors that larval *Drosophila* need for innocuous warming avoidance were not known.

Understanding homeostatic thermoregulation in larval *Drosophila* requires identifying the warming-responsive counterparts of the CCs and understanding how the outputs of CCs and WCs are combined to make behavioral decisions above, near, and below the homeostatic set point. Here, we uncover a new set of WCs and warming molecular receptors with close morphological and genetic similarity to the

[1]Department of Physics, Harvard University, Cambridge, MA 02138, USA. [2]Center for Brain Science, Harvard University, Cambridge, MA 02138, USA. [3]Systems, Synthetic, and Quantitative Biology PhD Program, Harvard University, Cambridge, Boston, MA 02115, USA. [4]Harvard College, Harvard University, Cambridge, MA 02138, USA. [5]National Center for Behavioral Genomics, Brandeis University, Waltham, MA 02454, USA. [6]Department of Biology, Brandeis University, Waltham, MA 02454, USA. [7]Volen National Center for Complex Systems, Brandeis University, Waltham, MA 02454, USA. [8]Janelia Research Campus, Howard Hughes Medical Institute, 19700 Helix Drive, Ashburn, VA 20147, USA. [9]University of Leipzig, Institute of Biology, Talstraße 33, 04103 Leipzig, Germany. [10]Department of Physiology, Development and Neuroscience, University of Cambridge, Downing Street, Cambridge CB2 3EG, UK. [11]MRC Laboratory of Molecular Biology, Cambridge Biomedical Campus, Francis Crick Avenue, Cambridge CB2 0QH, UK. [12]Department of Physics, University of Miami, Coral Gables, FL 33124, USA.
*Corresponding author. Email: luishernandeznunez@fas.harvard.edu (L.H.-N.); klein@miami.edu (M.K.); pgarrity@brandeis.edu (P.G.); samuel@physics.harvard.edu (A.D.T.S.)
†Present address: Facultad de Medicina, Universidad de la Republica, Av. Gral. Flores 2125, 11800 Montevideo, Departamento de Montevideo, Uruguay.

CCs and their molecular receptors. Using optogenetics, calcium imaging, precise temperature control, sensory receptor mutants, and quantitative behavioral analysis, we derive a sensorimotor transformation model that achieves homeostatic thermoregulation. This model implements ambient temperature context-dependent cross-inhibition between the simultaneous outputs of WCs and CCs. Flexible cross-inhibition allows the net effect of WC and CC outputs to drive cooling avoidance below 24°C, suppress avoidance to temperature changes near 24°C, and drive warming avoidance above 24°C. We use electron microscopy to reconstruct the wiring diagram of the WC and CC synaptic partners and connectome-based models to identify candidate circuits for implementing the cross-inhibitory sensorimotor transformation. Our study reveals how simultaneously active opponent sensors are integrated in a context-dependent manner to achieve homeostatic regulation.

RESULTS

Identifying WCs

To identify the warming-responsive counterparts of the CCs, we used in vivo calcium imaging. We expressed GCaMP6m (*13*) under the control of the *pebbled-Gal4* driver that labels all anterior sensory cells in the larva (*14*) (Fig. 1A). We subjected larvae to sinusoidal temperature waveforms, volumetrically imaged all anterior sensory ganglia, and used constrained non-negative matrix factorization (CNMF) (*15*) to analyze activity patterns for evidence of temperature-sensitive cells (Fig. 1B). CNMF uncovered two previously unidentified WCs in the DOG and identified the three previously described CCs (Fig. 1C). No other temperature-sensitive cells were apparent in any anterior sensory ganglia (fig. S1).

Thermosensory cells in many animals have specialized morphologies that presumably enhance temperature detection (*16*–*18*). We used confocal and electron microscopy to reconstruct the anatomy of the WCs and CCs to better understand their structural specializations. Both WCs and CCs are located in the DOG, which mostly contains olfactory receptor neurons that project to different glomeruli in the antennal lobe (AL) (*19*). We sought cell-specific labels for the WCs. CCs in both adult and larval *Drosophila* express ionotropic receptors (*20*–*22*). We screened Ir genes known to be expressed in the DOG and found that Ir68a-Gal4 exclusively labels the WCs (figs. S2 and S3 and Extended Methods). Cell-specific labeling of the WCs using green fluorescent protein (GFP) revealed that each WC projects to a distinct warming glomerulus (Fig. 1D). The CCs project to a single cooling glomerulus (*6*). All thermosensory glomeruli are located posterior and dorsal to the olfactory glomeruli.

The anatomy and location of the WCs and CCs facilitated their reconstruction using electron microscopy (Extended Methods). As in previous studies (*6*), we refer to the posterior CCs as A-CCs and to the most anterior CC as B-CC. The cell bodies and outer segments of the A-CCs and WCs are adjacent (Fig. 1E). The outer segments of the CCs and WCs have specialized morphologies, presumably containing signal transduction machinery. The CC outer segments are large and lamellated with heavily infolded plasma membranes. The WC outer segments are smaller and unlamellated (Fig. 1E, inset). These anatomical features are consistent with those of the WCs and CCs of adult *Drosophila* (*18*, *19*). The larval WCs, but not the CCs, also have a thin dendrite that protrudes to the surface of the olfactory dome (Fig. 1E, fig. S4, and Supplementary Materials). The cell body and outer segment of the B-CC are adjacent to a non-thermosensitive cell of the DOG (fig. S1 and Supplementary Materials).

The molecular basis of warming sensing

Because *Ir68a-Gal4* labels the WCs, we asked whether *Ir68a* might directly contribute to their thermosensitivity. Consistent with *Ir68a* expression in the WCs, a Gal4 reporter under the control of the endogenous *Ir68a* promoter ($Ir68a^{T2A\text{-}Gal4}$) drove cell-specific expression in the WCs. *Ir68a* was required for WC responsiveness to warming, as a loss-of-function mutation in *Ir68a* ($Ir68a^{PB}$) abolished temperature-evoked calcium dynamics in the WCs (Fig. 1F). The defect was specific, as cell-specific expression of wild-type *Ir68a* restored WC thermosensitivity in the $Ir68a^{PB}$ mutant (Fig. 1F).

Most ionotropic receptors in *Drosophila* appear to function as heteromers (*23*, *24*). In particular, the CCs require a set of three ionotropic receptors to respond to temperature changes: Ir21a, Ir93a, and Ir25a (*20*, *21*). We used $Ir21a^{T2A\text{-}Gal4}$ lines (*25*), in which Gal4 is expressed under the control of the endogenous Ir21a promoter, to drive GFP expression and found that Ir21a expression is specific to the CCs and was not detected in the WCs or elsewhere in the larva. For *Ir93a*, immunostaining revealed that the expression pattern of the Ir93a receptor is specific to the WCs and CCs (fig. S2). Ir25a is expressed in many anterior sensory cells including the WCs and CCs (*20*, *26*–*28*). Consistent with their expression in WCs, mutations disrupting either of these two receptors, Ir93a ($Ir93a^{MI}$) or Ir25a ($Ir25a^{2}$), abolished WC thermosensitivity (Fig. 1, G and H). The thermosensitivity of the WCs was restored in each mutant by cell-specific reexpression of the corresponding wild-type receptor (Fig. 1, G and H). No other known Ir receptors showed expression in WCs or CCs (Extended Methods).

Our results suggest a model in which distinct but overlapping sets of ionotropic receptors confer thermosensitivity to the WCs and CCs (Fig. 1I). Ir68a is specifically needed by the WCs to sense warming. Ir21a is specifically needed by the CCs to sense cooling. Ir93a and Ir25a are needed by both WCs and CCs to sense any temperature change. We further tested this model by ectopic expression of Ir68a and Ir21a in the CCs and WCs, respectively. Ectopic expression of Ir68a in the CCs diminished their sensitivity to cooling, while ectopic expression of Ir21a in the WCs transformed them into cooling sensors (Fig. 2). These findings support a model where Ir68a and Ir21a generate opposite thermosensitive polarities in WCs and CCs.

WCs and CCs are synchronous and opponent thermosensors

A first step to examine how WCs and CCs may be integrated to mediate homeostatic temperature control is to quantify their temperature-evoked neural dynamics. We labeled WCs and CCs with GCaMP6m and measured their calcium responses to warming or cooling step stimuli. A warming step evoked a transient increase in WC calcium levels and a transient decrease in CC calcium levels (Fig. 3A). A cooling step evoked a transient decrease in WC calcium levels and a transient increase in CC calcium levels (Fig. 3B). The average time for the calcium response peak (τ_{peak}) was not significantly different in WCs and CCs during warming or cooling steps (Fig. 3C). The time for adaptation of the neural response to baseline calcium levels ($\tau_{adaptation}$) was also not significantly different regardless of the polarity of the step stimulus (Fig. 3D). Thus, WCs and CCs are synchronous and bidirectional phasic sensors of temperature change with opposite polarity. WCs are activated by warming and inhibited by cooling, while CCs are activated by cooling and inhibited

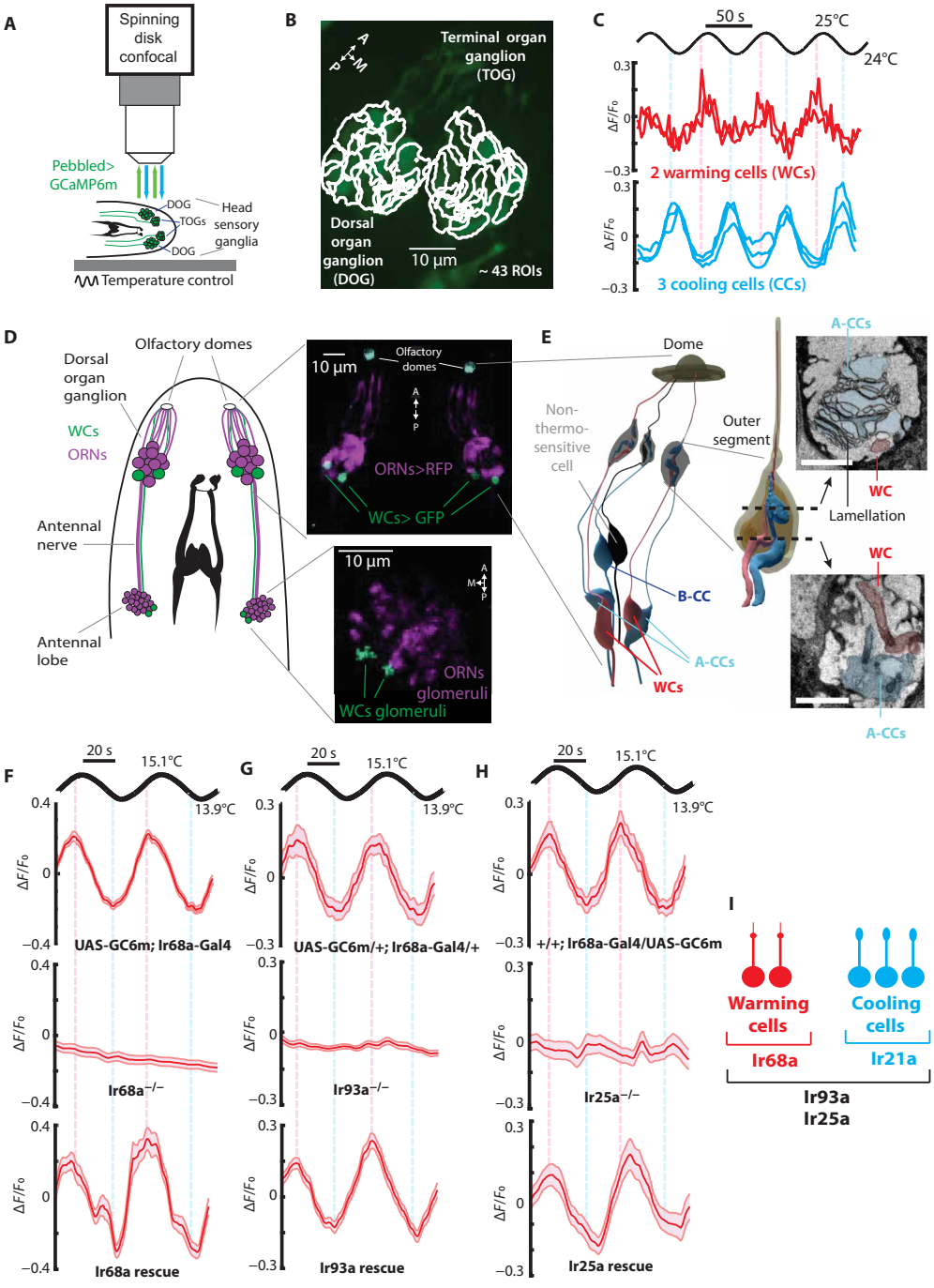

Fig. 1. The cellular and molecular basis of warming sensing. (**A**) Schematic representation of the larva head with all the anterior sensory organs expressing GCaMP6m via pebbled-Gal4 exposed to temperature sinusoidal fluctuations and imaged with a spinning disk confocal microscope (Genoype: w^{1118};Pebbled-Gal4/UAS-GCaMP6m, $n = 6$). (**B**) CNMF segmentation of the regions of interest (ROIs) in the *Drosophila* larva's head expressing GCaMP6m in the DOG and terminal organ ganglion (TOG). (**C**) Responses recovered via CNMF of the CCs (in cyan) and the new WCs (in red). (**D** and **E**) Anatomy of the WCs. (D) Larvae expressing GFP in the WCs and red fluorescent protein (RFP) in the olfactory receptor neurons (UAS-GFP;Ir68a-Gal4/orco-RFP) imaged in the DOG (cell bodies) and the antennal lobe (AL; axon terminals). (E) Electron microscopy reconstruction of the thermosensory dendritic bulbs shared by CCs and WCs (scale bars, 1 µm). The top inset shows a section in the lamellated outer segment, and the bottom inset shows an unlamellated part of WC and CC dendritic processes before the outer segment. (**F** to **H**) Ir68a, Ir93a, and Ir25a are required for warming sensing. Fluorescence changes in the WCs of larvae with different genotypes exposed to a sine wave of temperature. (F) Wild type: UAS-GCaMP6m;Ir68a-Gal4 ($n = 8$ animals), Ir68a defective mutants: UAS-GCaMP6m;$Ir68a^{PB}$,Ir68a-Gal4 ($n = 8$ animals), and Ir68a rescue: UAS-GCaMP6m;($Ir68a^{PB}$,Ir68a-Gal4)/($Ir68a^{PB}$,UAS-Ir68a) ($n = 10$ animals). (G) Wild type: UAS-GCaMP6m/+;Ir68a-Gal4/+ ($n = 8$ animals); Ir93a defective mutants: UAS-GCaMP6m;$Ir93a^{MI05555}$, Ir68a-Gal4/$Ir93a^{MI05555}$ ($n = 14$ animals); and Ir93a rescue: UAS-CaMP6m/+;(Ir93aiptMI05555, Ir68a-Gal4)/($Ir93a^{MI05555}$, UAS-Ir93a) ($n = 8$ animals). (H) Wild type: +;Ir68a-Gal4/UAS-GCaMP6m ($n = 8$ animals), Ir25a defective mutants: $Ir25a^{2}$;Ir68a-Gal4/UAS-GCaMP6m ($n = 20$ animals), and Ir25a rescue: (Ir25aBAC, $Ir25a^{2}$)/$Ir25a^{2}$;Ir68a-Gal4/UAS-GCaMP6m ($n = 20$ animals). Shaded regions are SEMs. (**I**) Warming and cooling receptor and co-receptor summary.

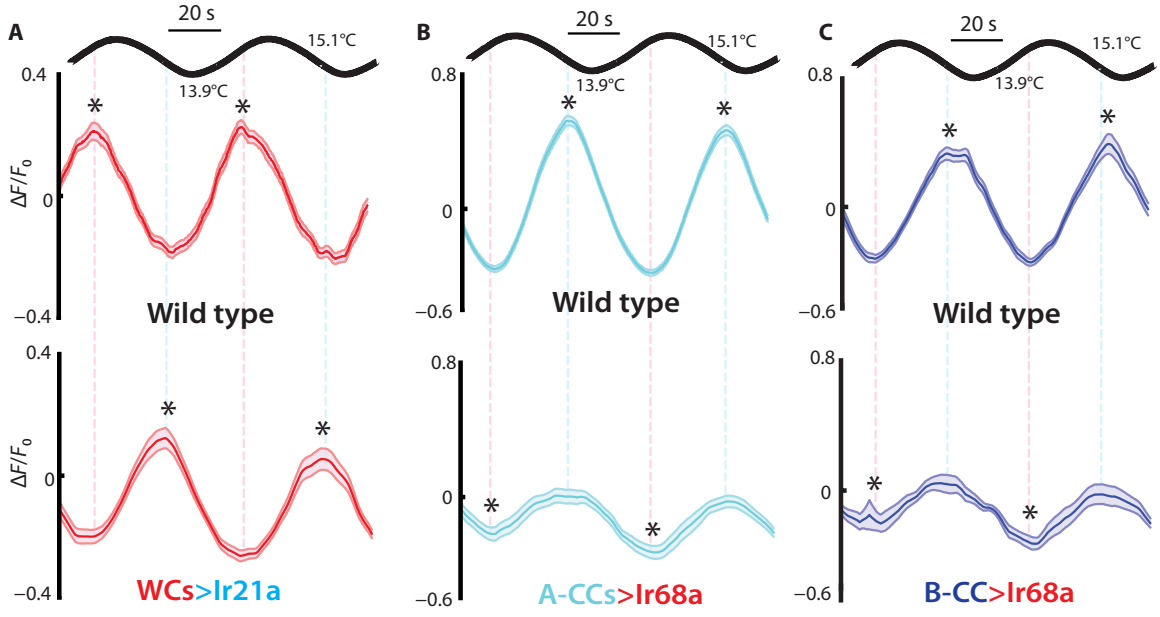

Fig. 2. Ectopic expression of opposed receptors. (**A**) Ectopic expression of Ir21a in the WCs inverts their polarity by transforming them into cooling-activated sensors. (Genoype: w^{1118};UAS-Ir21a;Ir68a-Gal4, UAS-GCaMP6m, $n = 8$). (**B** and **C**) Ectopic expression of Ir68a in the CCs attenuates their cooling response. (Genoype: w^{1118};R11F02-Gal4; UAS-Ir68a/UAs-GCaMP6m, $n = 6$). Shaded regions are SEMs. The asterisk indicates that the neural responses of the same color are different with Kruskal-Wallis test $P < 0.01$ during cooling or warming.

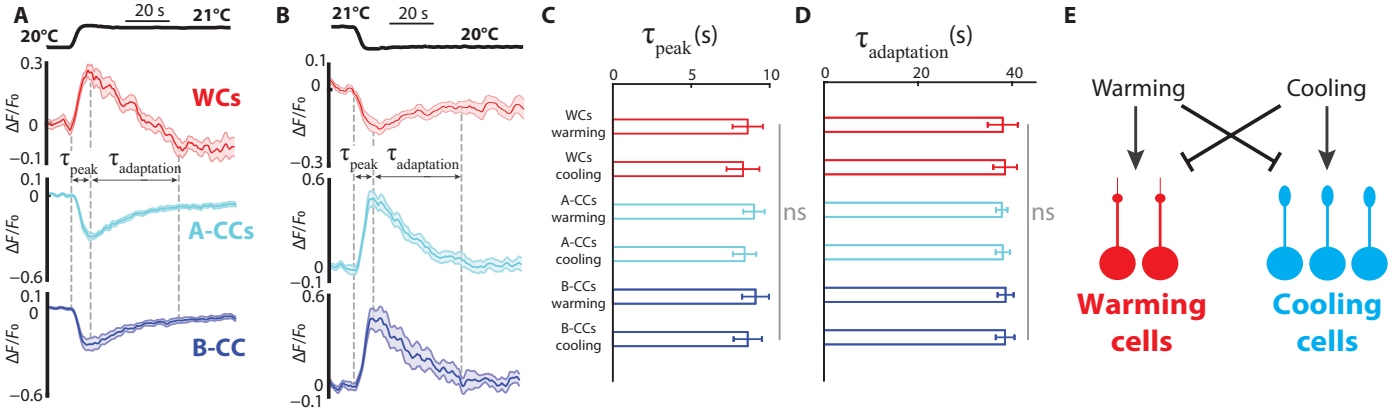

Fig. 3. Synchronous and opponent sensors of temperature change. (**A** and **B**) *Drosophila* larvae expressing GCaMP6m in the WCs (UAS-GCaMP6m;Ir68a-Gal4) or CCs (R11F02-Gal4;UAS-GCaMP6m) calcium responses to a 1°C temperature increase (A) or decrease (B). [WC responses are in red with $n = 12$ larvae, and CC responses are in cyan (A-CCs) and blue (B-CCs) with $n = 10$; the shaded regions are SEMs.] (**C**) The peak times of WC and CC responses to the warming and cooling step stimuli are not significantly different (Kruskal-Wallis test; error bars are SEMs). (**D**) The adaptation times of WC and CC responses to the warming and cooling step stimuli are not significantly different (Kruskal-Wallis test; error bars are SEMs). The gray "ns" in (C) and (D) indicates no statistically significant difference. (**E**) WCs are activated by warming and inhibited by cooling. CCs are inhibited by warming and activated by cooling.

by warming (Fig. 3E). The WCs and CCs also display these response properties when stimulated with sinusoidal temperature variations (fig. S5).

Behavioral flexibility is not solely encoded in WC or CC neural responses

The homeostatic temperature set point of first- and second-instar larval *Drosophila* is near 24°C. To achieve thermoregulation, larvae must flexibly interpret warming and cooling in different ambient temperature contexts (below, near, or above the set point). Understanding this flexibility requires mapping the interplay between temperature change, thermosensory neuron activity, and behavioral responses at different ambient temperatures. To do this, we developed a temperature control technique to deliver the same temperature waveforms at multiple ambient temperatures during calcium imaging and behavioral experiments (Fig. 4, A and B; fig. S6; and Extended Methods). We used this setup to quantify the temperature-evoked responses of freely behaving second-instar larvae.

Larval *Drosophila* navigate by alternating periods of forward crawling called runs and reorientation events called turns (Fig. 4C) (*29*). Using an unsupervised classifier to segment behavioral sequences (fig. S7 and Extended Methods), we found that turning

rate (the probability of turning per time unit) is the motor program most significantly modulated by temperature changes (figs. S7 and S8 and Extended Methods). Other navigation parameters—turn duration and number of head sweeps per turn—are also modulated by temperature. However, these additional parameters are correlated with turn rate and are less sensitive to temperature changes (fig. S9). Turn rate captures the valence, dynamics, and intensity of the behavioral response to a temperature stimulus (*6*, *29*, *30*).

To analyze how cooling and warming modulate turning rate at different ambient temperatures, freely moving larvae were exposed to identical sinusoidal waves of 1.2°C amplitude centered at temperatures below (14.9°C), near (23.9°C), or above (30.6°C) the homeostatic

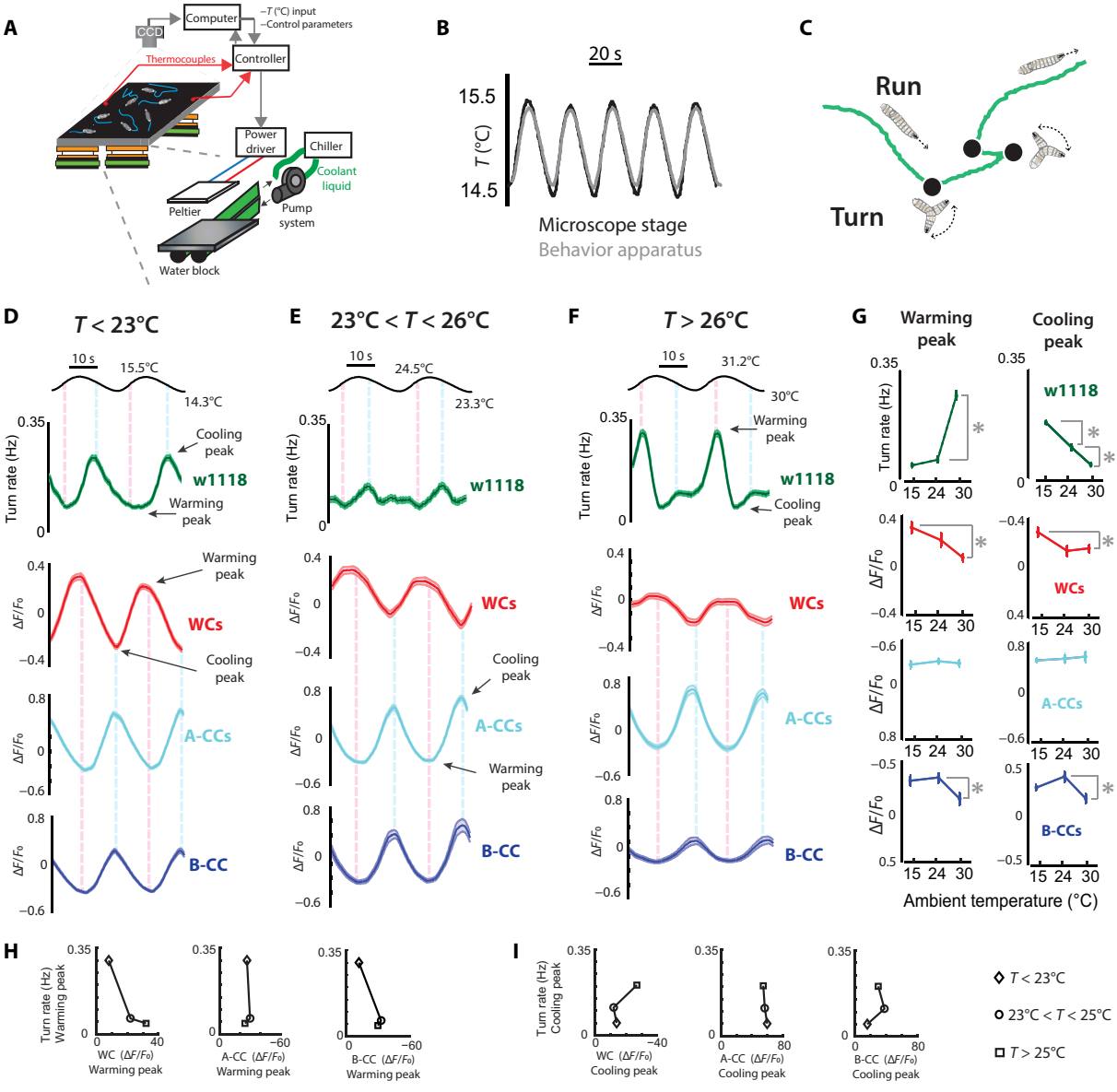

Fig. 4. Behavioral flexibility is not solely encoded in WC or CC neural responses. (**A**) Temperature control apparatus to study larval behavior. Four thermoelectric elements heat or cool a copper plate; rectangular agar is deposited on the copper plate, and larva crawl is deposited on the agar. CCD, charge-coupled device. (**B**) Sinusoidal waves of temperature measured on the behavior rig (in gray) and on the microscope stage (in black). (**C**) Larvae navigate by alternating periods of forward crawling called runs (green lines) and reorientation events called turns (black dots). (**D** to **F**) Behavioral and neural responses to sinusoidal temperature fluctuations below (D), near (E), and above (F) the homeostatic set point. First row: Experimental results of the turning rate responses of wild-type larvae (w^{1118} in green; shaded regions are SEMs; $n = 80$, 50, and 62 animals from left to right). Second row: Fluorescence changes in the WCs of Ir68a-Gal4;UAS-GCaMP6m larvae (red curves, $n = 8$ to 10 animals; shaded regions are SEMs). Third row: Fluorescence changes in the A-CCs of R11F02-Gal4;UAS-GCaMP6m larvae (cyan curves, $n = 7$ to 10 animals; shaded regions are SEMs). Fourth row: Fluorescence changes in the B-CCs of R11F02-Gal4;UAS-GCaMP6m larvae (blue curves, $n = 7$ to 10 animals; shaded regions are SEMs). (**G**) Summary of the peak behavioral and neural responses to cooling and warming. The "peaks" are the behavioral and neural response maximum or minimum values during cooling or warming. The error bars are SEMs of the behavioral or neural responses in (D) to (F). The asterisks indicate that the peak responses between the brackets are different with Kruskal-Wallis test $P < 0.01$. The absence of an asterisk between two data points indicates no statistically significant difference in (G). (**H** and **I**) The WC and CC peak responses to warming (H) and cooling (I) versus the peak behavioral responses at all ambient temperatures.

set point. Below the set point, turning rate peaks during the cooling phase (Fig. 4D), consistent with cooling avoidance behavior. Near the set point, avoidance responses are suppressed (Fig. 4E). Above the set point, turning rate peaks during the warming phase (Fig. 4F), consistent with warming avoidance behavior. Thus, warming and cooling are interpreted differently at different ambient temperatures.

We asked whether the flexible computation that transforms warming and cooling into behavior reflects differences in the sensitivity of WCs and CCs at different ambient temperatures. We tested the WC and CC neural responses to the same sinusoidal waves used to measure behavioral responses. Near the homeostatic set point, where avoidance behavioral responses are suppressed, WCs are activated during the warming phase and inhibited during the cooling phase, whereas the CCs are activated during the cooling phase and inhibited during the warming phase (Fig. 4E). Although neither temperature change should evoke avoidance near 24°C, WCs and CCs still display strong, opponent physiological responses to temperature change in this range. At all ambient temperatures, the CCs are activated by cooling and inhibited by warming (Fig. 4, D to G). The response amplitude of the B-CCs decreases at high temperatures but not at intermediate temperatures (Fig. 4, D to F). Thus, the CCs do not become specifically more sensitive at low temperatures to up-regulate cooling avoidance (Fig. 4I). Similarly, the WCs are activated by warming and inhibited by cooling at all temperatures (Fig. 4, D to G). The WCs are even more responsive at low temperatures and equally responsive at intermediate and high temperatures (Fig. 4G). Likewise, the WCs do not become specifically more sensitive at high temperatures to up-regulate warming avoidance (Fig. 4H). Therefore, the flexibility in the computation underlying thermal homeostasis is not primarily encoded in the physiological thermosensitivity of WCs and CCs.

Candidate computations underlying thermal homeostasis

How may the WC and CC neural responses contribute to the computation for thermal homeostasis? Answering this question requires mathematical modeling of the transformation from WC and CC neural activity into motor responses. We sought a sensorimotor transformation model for homeostatic thermoregulation. This type of model does not represent a neural circuit; it describes the computation the brain performs to transform current and past sensory neuron activity into motor responses and, thus, guides and constrains circuit-level implementations of sensory processing.

To begin building a sensorimotor transformation model, we start by assuming that the full behavioral output can be explained in terms of WC and CC neural responses. In later sections, we revisit this assumption and update the model accordingly.

Previous studies in *C. elegans*, larval *Drosophila*, and larval zebrafish were successful at using linear filters to describe sensorimotor transformations for navigational behaviors (*8*, *30*, *31*). Linear filters enable a mathematical and graphical representation of the temporal integration of neural activity that precedes a motor action. We sought to understand the temporal integration of WC and CC neural activity that precedes turns. Following a method that we previously developed (*30*), we used optogenetic white noise to stimulate either WCs or CCs while recording the posture of freely moving larvae. We then used reverse-correlation analysis to calculate the filters that transform WC or CC activity into turning rate (Fig. 5A and Extended Methods). Both filters were biphasic. Biphasic filters indicate that behavioral responses depend on the time derivative of WC or CC activity and not on their absolute activity levels (Fig. 5B). Both filters have similar shapes. The WC filter is not statistically distinct at any time point from the CC filter (Wilcoxon matched test with $P < 0.05$). These results suggest that functionally similar pathways transform the activities of WCs and CCs into behavior.

While the linear filters estimate how neural activity of WCs and CCs separately contribute to behavior, they do not establish how the simultaneous activity of WCs and CCs may combine to mediate behavioral responses to temperature changes. This can be determined using a linear combination model. Any candidate linear model for combining WC and CC activity to produce behavior is fully determined by knowing how sensory inputs map to WC and CC activity, how WC and CC activities separately map to turning rates, and how sensory inputs map to turning rates. Our datasets include all of these measurements. Next, we use these measurements to determine the architecture of the model and the scalar weights (w_{WC} and w_{CC}) that quantify the magnitude of WC and CC contributions to turning rate responses.

In principle, there are only three symmetric model architectures posited to integrate WC and CC outputs. In the labeled lines model (LLM), the WCs exclusively drive behavior during warming, and the CCs exclusively drive behavior during cooling (Fig. 5C). Alternatively, not only might WC and CC activation promote turning, but WC inhibition during cooling and CC inhibition during warming could also influence behavior. The polarity of such cross-modulation could be either negative in a cross-inhibition model (C-IM) (Fig. 5F) or positive in a cross-activation model (C-AM) (Fig. 5I).

In all candidate models, to simplify their graphical representation, we separate the predicted turning responses in "turning during cooling" and "turning during warming." The neural responses of WCs and CCs to temperature stimuli can be captured with linear filters (fig. S10), and for simplicity, we represent them with those filters in Fig. 5. However, in the calculations, we use the experimentally measured calcium responses of Fig. 4. A baseline turning rate of 0.05 Hz is a constant added to the output of the models (Fig. 5, C, F, and I).

In each of the three alternative architectures, the only free variables are the weights of the outputs of the WCs (w_{WC}) and the CCs (w_{CC}) at different ambient temperatures. For each architecture, we used linear regression analysis to predict the weights that best account for the behavior of wild-type larvae. In the LLM (Fig. 5C), below and near the homeostatic set point, w_{WC} must be zero to prevent an increase in turning during warming, while w_{CC} must scale the magnitude of turning during cooling (Fig. 5, D and E, left and center). Above the set point, w_{WC} scales the magnitude of turning during warming and w_{CC} must be zero to prevent an increase in turning during cooling (Fig. 5, D and E, right). With appropriate values of w_{WC} and w_{CC}, the LLM can be made consistent with behavior in all contexts ($R^2 > 0.79$).

In the C-IM (Fig. 5F), below the homeostatic set point, CC output is weighted more strongly than WC output to allow a net increase in turning during cooling (Fig. 5, G and H, left). Near the set point, w_{WC} and w_{CC} values are not zero (like in the LLM) but are balanced so that the mutual inhibition of both pathways results in attenuated turning rates (Fig. 5, G and H, center). Above the set point, WC output is weighted more strongly than CC output to allow a net increase in turning during warming (Fig. 5, G and H, right). With appropriate values of w_{WC} and w_{CC}, the C-IM can also be made consistent with behavior in all contexts ($R^2 > 0.68$).

In the C-AM (Fig. 5I), both WC and CC outputs regulate turning rate positively. As in the LLM, w_{WC} has to be zero below and near

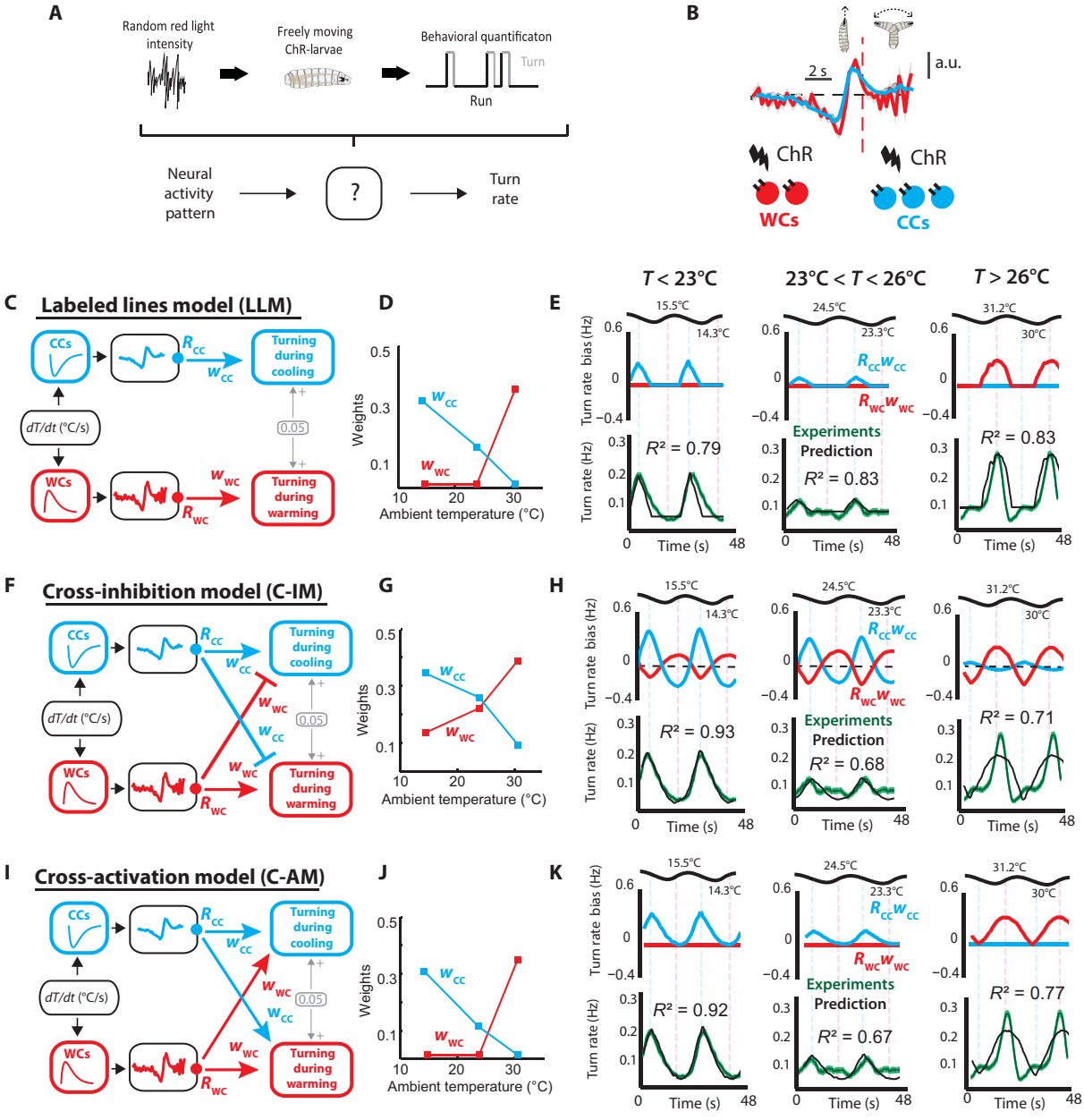

Fig. 5. Candidate computations underlying thermal homeostasis. (**A**) Mapping sensory neuron activity patterns to behavior. (**B**) Linear filters obtained with white noise optogenetic stimulation of WCs (curve in red) and CCs (curve in cyan). a.u., arbitrary units. We abbreviated CsChrimson as ChR. (**C**, **F**, and **I**) Schematic representation of the candidate computations underlying thermal homeostasis. The WC and CC outputs are convolved with behavior filters (Extended Methods), and the filter outputs (R_{CC} and R_{WC}) are then combined linearly with the scalar weights w_{CC} and w_{WC}. There are three possible symmetric architectures that linearly combine the outputs of WCs and CCs: (i) the labeled lines model (LLM) (C), (ii) the cross-inhibition model (C-IM) (F), and (iii) the cross-activation model (C-AM) (I). (**D**, **G**, and **J**) We used linear regression to obtain the weights w_{CC} and w_{WC} in each model architecture. (**E**, **H**, and **K**) First row: The outputs of the behavioral filter of the warming pathway (R_{WC}) and the cooling pathway (R_{CC}), scaled by their respective weights (w_{WC} and w_{CC}). Second row: Experimental results of the turning rate response to sine waves of temperature of wild-type larvae (w^{1118} in green) and model predictions (in black). Shaded regions around the green curve are SEMs. Correlation coefficients between the model predictions and experimental results are reported in each curve.

the homeostatic set point to prevent turning increases during warming, while w_{CC} has to scale the magnitude of turning during cooling (Fig. 5, J and K, left and center). Above the set point, w_{WC} scales the magnitude of turning during warming and w_{CC} has to be zero to prevent an increase in turning during cooling (Fig. 5, J and K, right). The C-AM can also be made consistent with behavior in all contexts ($R^2 > 0.67$).

All candidate models can be made consistent with wild-type larval *Drosophila* behavior at all ambient temperatures, albeit with different values of the weights of the WC and CC outputs. In each model, behavioral flexibility is encoded in the values of the weights (w_{WC} and w_{CC}) at different ambient temperatures. Determining which model represents the actual computation underlying thermal

homeostasis requires independent manipulation of the neural activity of WCs and CCs at all ambient temperature contexts.

Flexible cross-inhibition underlies thermal homeostasis

Thermosensory stimuli simultaneously affect both WC and CC activity, confounding attempts to distinguish the behavioral consequences of WC versus CC activity increases or decreases in different ambient temperature contexts. To independently manipulate WC or CC activity, we turned to optogenetics. Using controlled optogenetic illumination with cell-specific expression of CsChrimson (*32*) in either WCs or CCs, we separately induced fictive temperature changes onto each cell type at different ambient temperatures and compared model predictions with experimental results.

We found that increasing optogenetic stimulation of WCs (fictive warming) caused an increase in turning rate at all ambient temperatures (Fig. 6A). This result supports the C-IM, where activation of WCs causes increases in turning rates at all temperatures. In contrast, the LLM and the C-AM fail to predict the turning rate increase caused by WC activation below and near the homeostatic set point (Fig. 6A). Decreasing optogenetic stimulation of WCs (fictive cooling) caused a decrease in turning rate at all ambient temperatures (Fig. 6B). This also supports the C-IM, where a decrease in WC activity inhibits turning rates at all temperatures. The LLM fails to predict turning rates at all temperatures, and the C-AM fails to predict turning rates below and near the homeostatic set point (Fig. 6B).

We observed an opposite pattern with the CCs. Decreasing optogenetic stimulation of the CCs (fictive warming) caused a decrease in turning rate at all temperatures (Fig. 6C). This supports the C-IM, where a decrease in CC activity inhibits turning rate at all temperatures. The LLM fails to predict turning rates at all temperatures, and the C-AM fails to predict turning rates above the homeostatic set point (Fig. 6C). Last, increasing optogenetic stimulation of CCs (fictive cooling) caused an increase in turning rate (Fig. 6D). This also supports the C-IM model that predicts that CC activity increases are reflected in turning rate increases at all temperatures. The LLM and the C-AM fail to predict turning rates near or above the homeostatic set point. Control animals exhibited no behavioral responses to changes in optogenetic stimulation (Fig. 6E).

The C-IM is the only linear model that captures the contribution of WCs and CCs to thermoregulation in all contexts (Fig. 6F). This cross-inhibition does not operate with fixed weights because the flexibility needed to interpret warming and cooling in different ambient temperature contexts is not encoded in the neural responses of WCs and CCs. Instead, the flexibility of the cross-inhibition computation is encoded in the changing values of the weights (w_{WC} and w_{CC}) that appropriately scale the contribution of warming and cooling pathways.

Cross-inhibition computations in mutant larvae

The C-IM explains how the WC and CC outputs contribute to thermoregulation at different ambient temperatures. We showed in Fig. 5 that the C-IM can explain behavioral dynamics at all ambient temperature contexts in terms of WC and CC outputs. However, it is possible that other unknown thermosensory pathways also contribute to warming and cooling avoidance. Here, we investigate the roles of WCs and CCs in different temperature contexts using transgenic larvae with nonfunctional mutations for warming receptors ($Ir68a^{PB}$), cooling receptors ($Ir21a^{123}$), or both ($Ir93a^{MI}$). We update the C-IM on the basis of our findings and show that it can explain the deficits in thermoregulation caused by mutations that render WCs or CCs nonfunctional.

Inactivating the WC and CC pathway via the $Ir93a^{MI}$ mutation resulted in attenuated cooling avoidance below the homeostatic set point, attenuated warming avoidance above the set point, and thermal blindness near the set point (Fig. 7A, bottom row). Because $Ir93a^{MI}$ larvae were not thermally blind at all ambient temperatures, there appear to be parallel thermosensory pathways that operate far from the set point. This does not invalidate the C-IM, as the optogenetic results used to validate it are unaffected by this finding. We incorporated these new results to the C-IM by combining linearly the turning rate responses of $Ir93a^{MI}$ mutant larvae (the contribution of potential parallel pathways) with the output of the C-IM (Fig. 7A, top row). This adjustment only requires rescaling the C-IM output by a constant applied to the weights w_{WC} and w_{CC} at low and high ambient temperatures (Methods and Extended Methods). Near the set point, where no other pathway contributes to temperature-evoked turning responses or homeostatic thermoregulation, the C-IM needs no adjustment.

The updated C-IM captures wild-type behavior as well as the initial model with correlation coefficients between 0.68 and 0.91 (Fig. 7B). The updated model predicts that, below the homeostatic set point, turning during cooling is strongly stimulated by the CCs and moderately cross-inhibited by the WCs, resulting in a net increase in turning during cooling (Fig. 7A-I). Near the set point, turning during warming and cooling is mutually inhibited by the WCs and CCs, resulting in lower turning rates (Fig. 7A-II). Above the set point, turning during warming is strongly stimulated by the WCs and moderately cross-inhibited by the CCs, resulting in a net increase in turning during warming (Fig. 7A-III).

Using the updated C-IM to predict how mutations that render the WCs or CCs nonfunctional may affect thermoregulation and experiments with mutant larvae, we elucidate the different roles of WCs and CCs at different ambient temperatures. The updated C-IM predicts that larvae without functional WCs will have reduced cross-inhibition of turning during cooling and reduced turning during warming (Fig. 7C). The absence of cross-inhibition during cooling is predicted to be more noticeable at low and medium temperatures (Fig. 7, C-I and C-II), while the absence of WC-driven turning during warming is predicted to be more noticeable at high temperatures (Fig. 7C-III). As predicted, larvae without functional WCs (via the $Ir68a^{PB}$ mutation) present significantly reduced turning during warming above the homeostatic set point (Fig. 7C-III) and significantly increased turning during cooling (consistent with significantly reduced cross-inhibition of turning during cooling) near and below the homeostatic set point (Fig. 7, C-I and C-II). The model predicts the behavior of larvae without functional WCs with correlation coefficients between 0.65 and 0.86 (Fig. 7D).

Similarly, the updated C-IM predicts that larvae without functional CCs have reduced cross-inhibition of turning during warming and reduced turning during cooling (Fig. 7E). The absence of cross-inhibition during warming is predicted to be more noticeable at medium temperatures and more moderate at high temperatures (because of the low weight of the CC contribution to behavior at high temperatures) (Fig. 7, E-II and E-III), while the absence of CC-driven turning during cooling is predicted to be more noticeable at low and medium temperatures (Fig. 7, E-I and E-II). As predicted, larvae without functional CCs (via the $Ir21a^{123}$ mutation) present significantly reduced turning during cooling below and near the

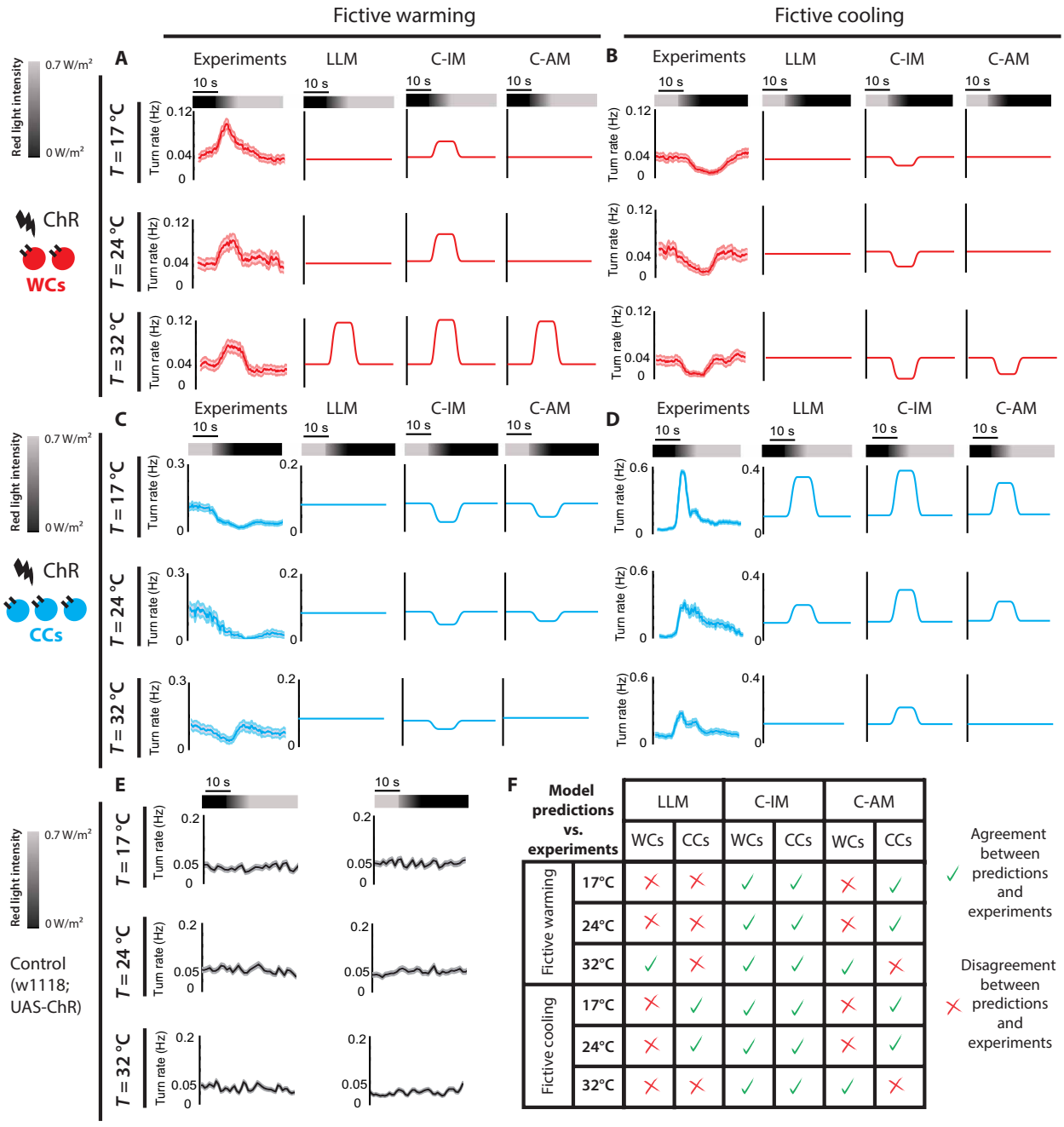

Fig. 6. Flexible cross-inhibition underlies thermal homeostasis. (**A**) Optogenetic fictive warming of WCs. First column: Turning rate of larvae expressing the red-shifted optogenetic channel CsChrimson (ChR) in the WCs (w^{1118};UAS-CsChrimson/+;Ir68a-Gal4/+) exposed to positive ramps of red light (fictive warming) at all ambient temperatures. Other columns: Model-predicted turning rates in response to a ramp increase of WC activity. (**B**) Optogenetic fictive cooling of WCs. First column: Turning rate of larvae expressing the red-shifted optogenetic channel CsChrimson (ChR) in the WCs (w^{1118};UAS-CsChrimson/+;Ir68a-Gal4/+) exposed to negative ramps of red light (fictive cooling) at all ambient temperatures. Other columns: Model-predicted turning rates in response to a ramp decrease of WC activity. In (A) and (B), $n = 116$ to 125 animals for each ambient temperature and shaded regions are SEMs. (**C**) Optogenetic fictive warming of CCs. First column: Turning rate of larvae expressing the red-shifted optogenetic channel CsChrimson (ChR) in the CCs (w^{1118};UAS-CsChrimson/+;R11F02-Gal4/+) exposed to negative ramps of red light (fictive warming) at all ambient temperatures. Other columns: Model-predicted turning rates in response to a ramp decrease of CC activity. (**D**) Optogenetic fictive cooling of CCs. First column: Turning rate of larvae expressing the red-shifted optogenetic channel CsChrimson (ChR) in the CCs (w^{1118}; UAS-CsChrimson/+;R11F02-Gal4/+) exposed to positive ramps of red light (fictive cooling) at all ambient temperatures. Other columns: Model-predicted turning rates in response to a ramp increase of CC activity. In (C) and (D), $n = 90$ to 101 animals for each ambient temperature and shaded regions are SEMs. (**E**) Turning rate of control larvae (w^{1118}; UAS-CsChrimson/+) fed with all-trans-retinal and exposed to positive and negative ramps of red light. $n = 85$ to 120 animals at each ambient temperature, shaded regions are SEMs. (**F**) Summary chart of the agreement between model predictions and experimental results.

Model predictions vs. experiments		LLM		C-IM		C-AM	
		WCs	CCs	WCs	CCs	WCs	CCs
Fictive warming	17°C	✗	✗	✓	✓	✗	✓
	24°C	✗	✗	✓	✓	✗	✓
	32°C	✓	✗	✓	✓	✓	✗
Fictive cooling	17°C	✗	✓	✓	✓	✗	✓
	24°C	✗	✓	✓	✓	✗	✓
	32°C	✗	✗	✓	✓	✓	✗

✓ Agreement between predictions and experiments

✗ Disagreement between predictions and experiments

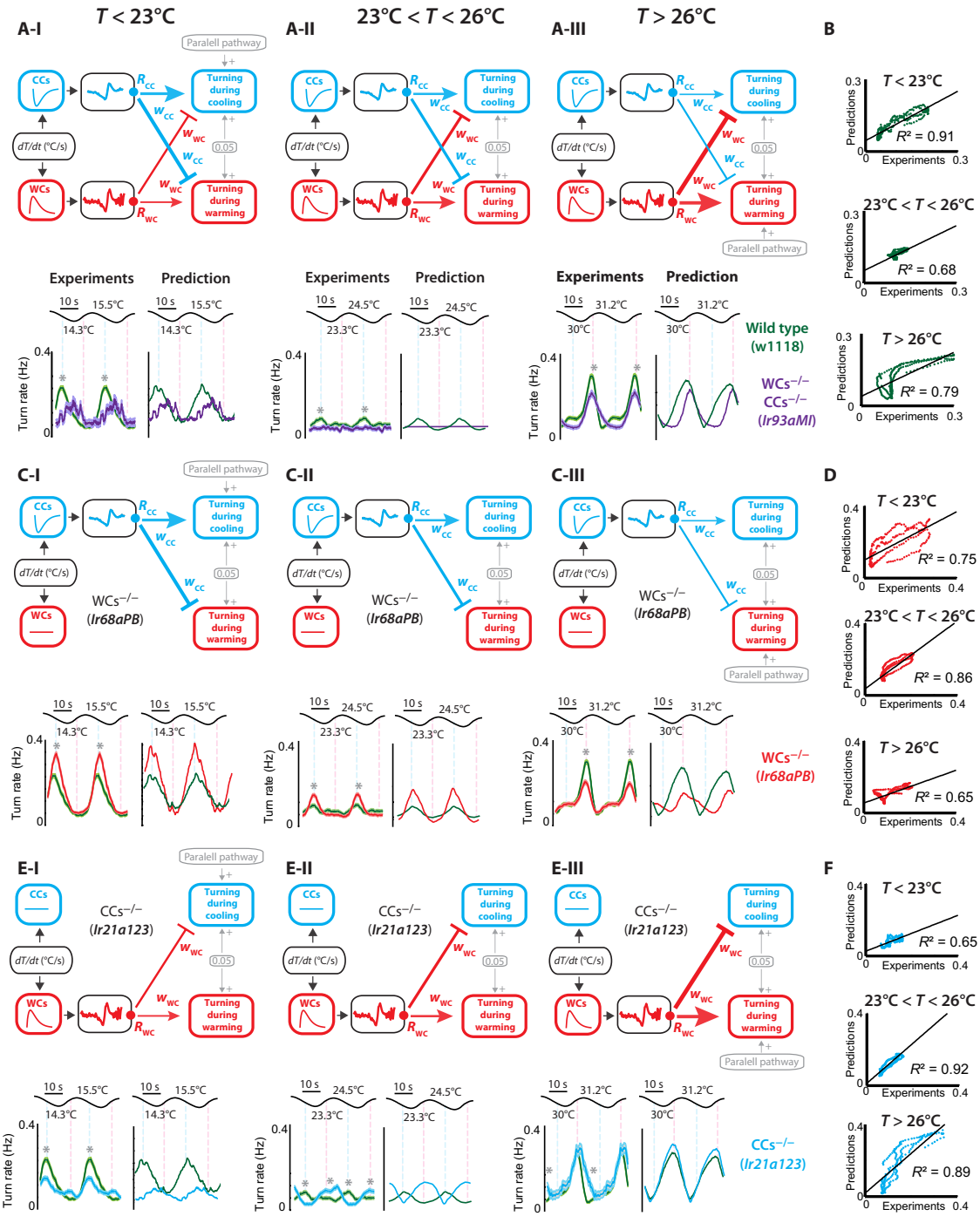

Fig. 7. Cross-inhibition computations in mutant larvae. (**A**) Top: Schematic representation of the model in wild-type larvae below (A-I), near (A-II), and above (A-III) the homeostatic set point. The lines that represent the contributions of WCs and CCs to warming and cooling turning, respectively, were drawn with a thickness that is proportional to the weights w_{WC} and w_{CC}. Bottom: Experimental results and model predictions of the turning rate responses of wild-type larvae (w^{1118} in green) and larvae defective for WCs and CC function (w^{1118}; $Ir93a^{MI05555}$ in purple). (**B**) Correlation between experiments and model predictions. (**C**) Top: Schematic representation of the model in larvae defective for WC function below (C-I), near (C-II), and above (C-III) the homeostatic set point. Bottom: Experimental results and model predictions of the turning rate responses of wild-type larvae (w^{1118} in green) and larvae defective for WC function (w^{1118}; $Ir68a^{PB}$ in red). (**D**) Correlation between experiments and model predictions. (**E**) Top: Schematic representation of the model in larvae defective for CC function below (E-I), near (E-II), and above (E-III) the homeostatic set point. Bottom: Experimental results and model predictions of the turning rate responses of wild-type larvae (w^{1118} in green) and larvae defective for CC function (w^{1118}; $Ir21a^{123}$ in cyan). (**F**) Correlation between experiments and model predictions. Shaded regions are SEMs. Asterisks indicate different mean turning rate during cooling or warming between the two overlaid turning rate responses in each panel using chi-square test with Bonferroni correction ($P < 0.005$). w^{1118} in green: $n = 80$ in (A-I), $n = 50$ in (A-II), and $n = 62$ in (A-III). w^{1118}; $Ir93a^{MI05555}$ in purple: $n = 42$ in (A-I), $n = 45$ in (A-II), and $n = 55$ in (A-III). w^{1118}; $Ir68a^{PB}$ in red: $n = 61$ in (C-I), $n = 59$ in (C-II), and $n = 55$ in (C-III). w^{1118}; $Ir21a^{123}$ in cyan: $n = 45$ in (E-I), $n = 54$ in (E-II), and $n = 49$ in (E-III).

homeostatic set point (Fig. 7, E-I and E-II) and significantly increased turning during warming (consistent with significantly reduced cross-inhibition of turning during warming) near the homeostatic set point (Fig. 7E-II). Above the homeostatic set point, the small increase in the peak value of turning during warming predicted by the model is not captured at the resolution of our experiments, but the overall likelihood of turning during warming is significantly higher in the $Ir21a^{123}$ mutant larvae than in wild-type larvae, as predicted by the model (Fig. 7E-III). The model predicts the behavior of larvae without functional CCs with correlation coefficients between 0.65 and 0.92 (Fig. 7F).

Together, our results demonstrate that larvae display warming and cooling avoidance behaviors with intensities that are precisely tuned by how far their body temperature is from their homeostatic set point (Fig. 7A). The intensities of these avoidance behaviors are maintained by the interplay of the positive and negative contributions of WCs and CCs to turning rate (Fig. 7, C and E). This phenomenon dominates behavior near the set point, where larvae with nonfunctional CCs display warming avoidance when they should not and larvae with nonfunctional WCs display a significant increase in cooling avoidance (Fig. 7, C-II and E-II). Our results show not only that the WC and CC pathways contribute to cooling avoidance at low temperatures and warming avoidance at high temperatures but also that both are needed to gradually adjust both avoidance behaviors as body temperature approaches the homeostatic set point.

Neural and behavioral encoding of warming and cooling speed

Next, we asked how the cross-inhibition computation affects, in addition to the polarity and intensity of neural activity and behavior, the temporal dynamics of these responses. Fast warming above the homeostatic set point would be expected to produce stronger turning responses than slow warming (*10*). Similarly, fast cooling below the homeostatic set point would be expected to produce stronger turning responses than slow cooling. We used the cross-inhibition model to formulate hypotheses about how the speeds of warming and cooling are encoded in neural and behavioral responses and tested these predictions experimentally.

In the cross-inhibition computation, WC and CC neural responses are passed through linear filters that transform them into the turning rate contributions R_{WC} and R_{CC} (Fig. 8, A and B, top). The linear filters are biphasic with both positive and negative parts. Biphasic filter outputs (R_{WC} and R_{CC}) are sensitive to the speed of their inputs (WC and CC neural responses). Thus, R_{WC} and R_{CC} are not correlated with WC and CC neural responses; they are correlated with the derivative of WC and CC neural responses (Fig. 8, A and B). In consequence, the cross-inhibition computation predicts that even temperature stimuli that produce similar amplitude of WC and CC neural activities can evoke behavioral responses of different magnitude if the time derivative of WC and CC neural activities changes.

We tested the predictions of the C-IM by delivering sinusoidal temperature waves of identical amplitude but different speeds and measuring the WC and CC calcium responses and the turning rate responses (Fig. 8, C and D). Fast and slow sinusoidal stimuli evoked WC and CC neural responses with equal amplitude but significantly different response derivatives (Fig. 8, C to E, top). Because the fast and slow stimuli are centered at a temperature below the set point, the model predicts that the WC and CC pathway contributes to an increase in cooling-evoked turning in both cases. Although the WC and CC neural responses have equal amplitudes, the model predicts a stronger behavioral response to the fast stimulus because the turning rate contributions R_{WC} and R_{CC} depend on the derivative of the neural responses (Fig. 8, C to E). As predicted, wild-type animals also display a stronger cooling avoidance response to the fast stimulus than to the slow stimulus (Fig. 8, C to E, bottom). The behavioral responses of mutant animals defective for WCs or CCs also follow the model predictions (fig. S11). The warming and cooling speed modulation of the behavioral responses was not caused by parallel thermosensory pathways, as the behavioral responses of larvae defective for WC and CC function (via the $Ir93a^{MI}$ mutation) to the fast and slow stimuli had not significantly different amplitudes (Fig. 8, C to E, bottom).

Another way in which the speed of warming and cooling can affect behavior is by direct modulation of the WC and CC neural response amplitudes. We tested this possibility at high temperatures, where the WCs are less responsive to temperature changes. In this temperature range, WCs can detect the fast stimulus but not the slow stimulus (Fig. 8, F to H, top), suggesting that the WCs are better tuned to detect rapid temperature changes. Consequently, the model predicts that WCs contribute to warming avoidance when exposed to fast stimuli but not when exposed to slow stimuli (Fig. 8, F to H). Consistent with the model, experiments with wild-type larvae revealed that the fast stimulus evoked stronger warming avoidance responses than the slow stimulus (Fig. 8, F to H, bottom). Mutants defective for WC function (via the $Ir68a^{PB}$ mutation) displayed diminished warming avoidance responses to the fast stimulus (Fig. 8F, bottom). Because WCs did not detect the slow stimulus, the warming avoidance response of larvae defective for WC function was identical to the one of wild-type larvae (Fig. 8, G and H, bottom). The behavioral responses of the other possible mutations for WC and CC function also follow the model predictions (fig. S11).

We conclude that the speed of warming and cooling is encoded in two ways: (i) in the neural circuits downstream of WCs and CCs represented by the biphasic linear filters that transform WC and CC neural activities into the turning contributions R_{WC} and R_{CC}, and (ii) in the intrinsic sensitivity of WCs and CCs to the speed of temperature change. Both types of encoding were experimentally validated using fast and slow stimuli that produce WC and CC neural activities with identical amplitudes but different time derivatives (Fig. 8, C to E) and using fast and slow stimuli that produce different amplitudes of WC and CC neural activities (Fig. 8, F to H).

WCs and CCs underlie thermal homeostasis

In many control systems, bidirectional fluctuations from a set point require bidirectional corrections in opposite directions. In human thermoregulation, physiological responses such as sweating or cutaneous vasoconstriction are used to compensate for small internal temperature increases or decreases, respectively. Do the WCs, CCs, and C-IM represent a homeostatic temperature control system at the level of larval *Drosophila* behavior by implementing bidirectional responses around a specific set point to control body temperature? Is homeostatic thermal regulation near the set point entirely mediated by the WCs and CCs?

We used the cross-inhibition model to identify the experimental conditions required for bidirectional control. In the cross-inhibition model, w_{WC} has larger values at higher ambient temperature, and w_{CC} has higher values at lower temperatures. To use the model to predict behavioral responses at ambient temperatures near the homeostatic

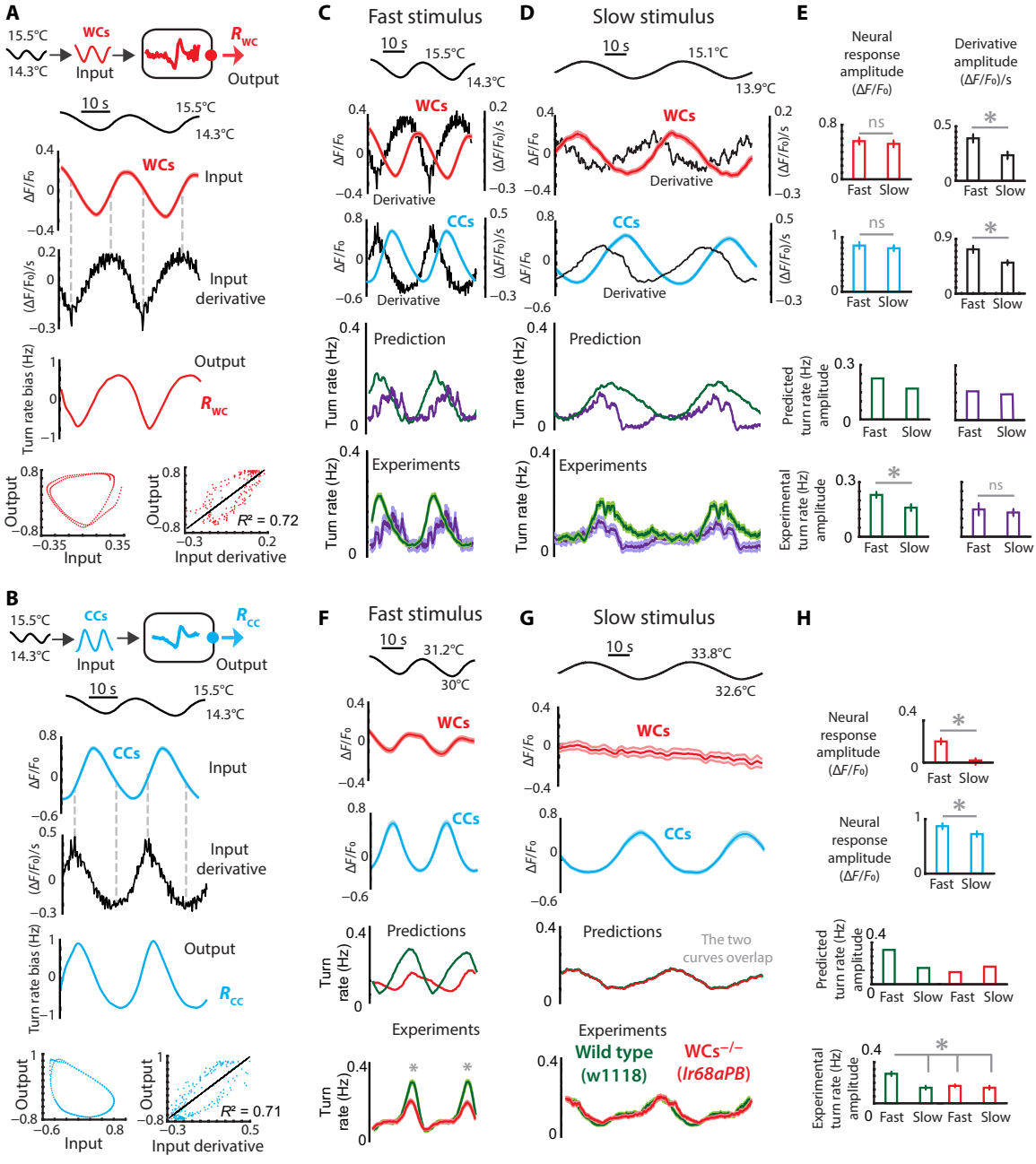

Fig. 8. Neural and behavioral encoding of warming and cooling speed. (**A** and **B**) Experimentally measured neural activities of WCs and CCs are the input of the C-IM. Linear filters transform neural activity into the turning rate contributions (R_{WC} and R_{CC}). The WC activity (Input) and its derivative (Input derivative) relate to the turning rate contribution R_{WC} (Output). The derivative of the WC activity is strongly correlated with R_{WC} (A). The CC activity (Input) and its derivative (Input derivative) relate to the turning rate contribution R_{CC} (Output). The derivative of the CC activity is strongly correlated with R_{CC} (B). (**C** to **E**) First two rows: Neural responses and their derivatives to slow and fast sinusoidal stimuli centered at low ambient temperatures. Third row: The model predicts different amplitudes of behavioral responses to the slow and fast stimuli. Fourth row: Following the trend of the model and the derivative of WC and CC activity, experimental results show that turning rate is significantly higher in response to the fast stimulus. (**F** to **H**) First two rows: Neural responses to slow and fast sinusoidal stimuli centered at high ambient temperatures. Third row: The model predicts stronger turning rate responses to the fast stimulus, largely due to the contribution of WCs. The green and red curves are identical in response to the slow stimulus (model predictions without functional WCs are in red; wild type, green). Fourth row: Experimental results follow model predictions, with the contribution of the WCs explaining the difference in turning rates elicited in response to the fast and slow stimuli. In all panels, the asterisks indicate that the peak responses between the brackets are different with Kruskal-Wallis test $P < 0.01$. The gray ns indicates no statistically significant difference, and the error bars are SEMs.

set point, we fitted linear functions that relate ambient temperatures with the values of w_{WC} and w_{CC}. Then, we used fast and slow sinusoidal stimuli as inputs to the model and calculated the predicted turning rates for ambient temperatures near the homeostatic set point (Fig. 9, A to C).

The predictions of our model reveal a temperature range around 24.5°C where bidirectional control occurs. Bidirectional control was not observed in Fig. 7C because the sinusoidal temperature wave did not surpass 24.5°C (Fig. 9C). Around 24.5°C, wild-type animals are predicted to increase their turning rate in response to both cooling and warming (Fig. 9D, green line). Mutants without WC function are predicted to display increased turning during cooling and baseline turning during warming (Fig. 9D, red line). Mutants without CC function are predicted to display increased turning during warming and baseline turning during cooling (Fig. 9D, cyan line). Mutants defective for both CCs and WCs are predicted to display no behavioral responses (Fig. 9D, purple line).

Experimental results validate all model predictions: Wild-type animals have increased turning during warming and cooling. Mutants defective for WC function have increased turning during cooling and do not modulate turning during warming. Mutants defective for CC function have increased turning during warming and do not modulate turning during cooling. Last, without WCs and CCs, there were no behavioral responses to temperature change (Fig. 9, E and F).

We conclude that both WCs and CCs are required for homeostatic temperature control. Missing one type of sensor results in avoidance to only warming or cooling and thus compromises the

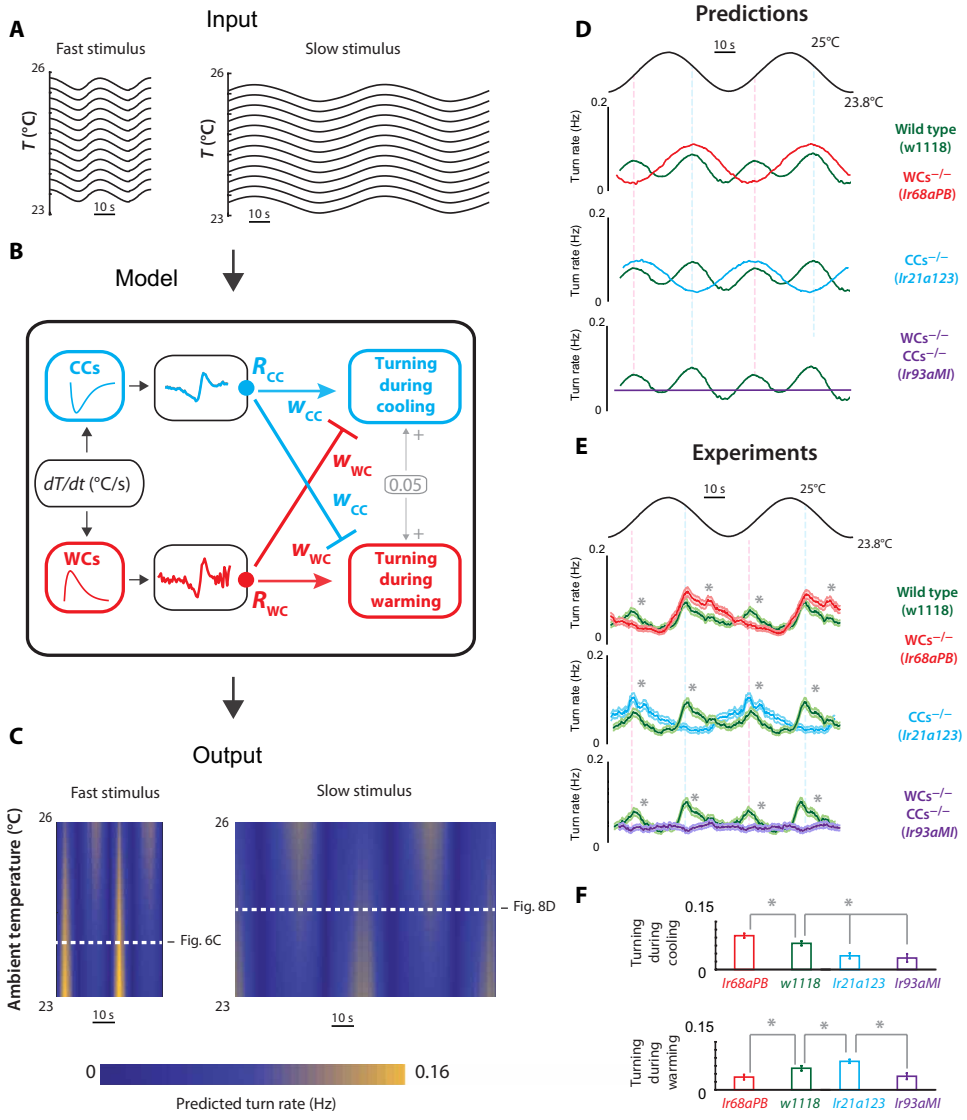

Fig. 9. WCs and CCs underlie thermal homeostasis. (**A**) Sinusoidal temperature stimuli at ambient temperatures near the homeostatic set point can be used as an input to the model. (**B**) To predict behavioral responses, we use linear filters to predict neural responses and we fit linear functions that relate the weights (w_{WC} and w_{CC}) to ambient temperature. (**C**) Using the C-IM, we predict the behavioral responses driven by the WC and CC pathway for stimuli at all ambient temperatures. (**D**) A stimulus centered at the homeostatic set point is predicted to drive turning increases during both cooling and warming. The turning during warming is driven by the WCs and cross-inhibited by the CCs. The turning during cooling is driven by the CCs and cross-inhibited by the WCs. (**E** and **F**) Experimental results validate all model predictions. In all panels, the asterisks indicate that the peak responses between the brackets are different with Kruskal-Wallis test $P < 0.01$. All error bars and shaded regions represent SEMs.

ability of larvae to stay at the homeostatic set point. The role of cross-inhibition is to scale the intensity of the avoidance responses to the adversity of the stimulus.

The wiring diagram of WC and CC synaptic partners

The cross-inhibitory model of sensorimotor transformation downstream of the WCs and CCs provides a quantitative representation of the underlying computation that transforms time-varying temperature changes into behavioral responses. How are the steps of this computation encoded in the properties of downstream neurons and neural circuits?

To start mapping the neural circuits for thermosensory processing, we turned to serial-section electron microscopy of the synaptic partners of the WCs and CCs. The small size of the larval *Drosophila* nervous system makes it amenable for connectomics. Using a complete volume of the central nervous system of a first-instar larva (*33*), we traced the connections between the WCs, CCs, and their synaptic partners at synaptic resolution (Fig. 10, A to D, and fig. S12A).

Second-order circuits of the thermosensory pathway

The WC axon terminals synapse with two types of second-order neurons, broad local neurons (bLNs) and bilateral warming projection neurons (bW-PNs) (Fig. 10A). bLNs lack an axon and conduct local computations in the AL (in gray in Fig. 10A). bW-PNs receive bilateral inputs from WCs and unilateral inputs from bLNs and send axons to the mushroom body calyx (in black in Fig. 10A). The bW-PNs also receive inputs from the Or33a-expressing olfactory receptor neurons. The bLNs are the same population of GABAergic interneurons that provide inhibition to all olfactory glomeruli in the AL. These connectivity patterns are consistent with early multisensory integration and suggest thermosensory normalization of olfactory information in the AL (fig. S12B).

The CC axon terminals do not synapse with any type of local neuron. Their only synaptic partners are five types of PNs: the cooling A and B-PN (C-AB-PN), the cooling A-PN (C-A-PN), the cooling B-PN (C-B-PN), the bilateral cooling-PN (bC-PN), and the integration-PN (I-PN) (Fig. 10C). The C-AB-PNs, C-A-PNs, and C-B-PNs are unilateral and project to the mushroom body calyx but receive different numbers of synapses from the A- and B-type CCs. C-AB-PNs receive a similar number of synapses from A- and B-type CCs. C-A-PNs receive synapses preferentially from the A-type CCs, and C-B-PNs receive synapses preferentially from the B-type CCs (fig. S12C). The bC-PNs together with the bW-PNs converge at the I-PN, which also receives inputs from the CCs, potentially integrating the warming and cooling pathways (Fig. 10, B and D).

Early feature extraction in the warming pathway

In the C-IM, the first step in the transformation from sensory neuron activity to turning responses is calculating the time derivative of WC and CC neural activity (Figs. 8 and 10E, left). We asked whether this calculation might be implemented in the second-order circuits of the thermosensory pathway.

The circuit downstream of the WCs shares the topology of the olfactory uniglomerular circuit (*34*). In this circuit topology, the inhibition from bLNs can tune the gain of the transformation of sensory neuron activity to PN activity (i.e., gain control), which can lead to PN encoding of the time derivative of the sensory neuron activity (*35*). To test this possibility, we built a firing rate model of the thermosensory circuit (Methods). This model predicted that the bW-PNs encode a time-derivative component of the WCs, as their maximum activity occurs during the rising phase of WC activity and their minimum activity occurs during the decaying phase of WC activity (Fig. 10E, center). Moreover, the predicted bW-PN activity and the C-IM internal variable R_{WC} (that represents the contribution of WCs to turning rate) are correlated with $R^2 = 0.82$.

To experimentally test the circuit model predictions, we searched the FlyLight database (*36*) for Gal4 drivers that label the bW-PNs. We found that the R78E05-Gal4 line labels neurons with similar anatomy to the bW-PNs. Using calcium imaging, we confirmed that the labeled neurons were responsive to warming (Fig. 10E, right). Their warming responses, consistent with the predictions of the circuit model, encode the WC derivative. The predicted and experimentally measured bW-PN responses are correlated with $R^2 = 0.79$, and the C-IM internal variable R_{WC} is correlated with the experimental bW-PN response with $R^2 = 0.74$.

These results suggest that the first step in the C-IM model, calculating the time derivative of WC activity, is carried out by a second-order circuit in the warming pathway. The bW-PNs encode the time derivative of WC neural activity.

Early integration of warming and cooling pathways

Our sensorimotor transformation model implies convergence of the warming and cooling pathways in determining turning responses. The I-PNs uncovered by the connectome directly integrate inputs from the warming and cooling bilateral PNs (bW-PN and bC-PN) and receive additional inputs from the CCs (Fig. 10, D and F). Our C-IM assigns flexible weights to the warming and cooling pathways, whereas the wiring diagram has fixed synaptic weights in the integration between warming and cooling pathways. Using a firing rate model with fixed synaptic weights and excitatory connections from the bilateral PNs to the I-PN, we predict that the I-PNs preferentially respond to cooling (Fig. 10F). This occurs because the I-PNs receive more inputs from the CCs and bC-PNs than from the bW-PNs (fig. S12). Future work on this circuit may clarify whether the flexibility of warming and cooling integration happens in this circuit (e.g., through nonsynaptic neuromodulatory mechanisms) or in downstream layers of the thermosensory circuit.

DISCUSSION

In thermosensation, often one type of sensor (cooling or warming) is studied without its counterpart, making our understanding of the computations' underlying thermal homeostasis incomplete (*6*, *21*, *37*). The justification for studying thermosensory cells' function without their counterparts is based on the "labeled line" hypothesis, in which cells activated by cooling exclusively regulate mechanisms that counteract cooling and cells activated by warming exclusively regulate mechanisms that counteract warming (*38*–*40*). In this view, the outputs of WCs and CCs do not necessarily integrate to shape thermoregulatory responses.

Here, we discovered novel larval *Drosophila* WCs and their warming molecular receptors (Ir68a, Ir93a, and Ir25a). We found that these WCs, together with their CC counterparts, underlie the behavioral mechanism for thermal homeostasis near the larva's set point. We have elucidated the computation that uses WC and CC outputs to determine the larva's turning responses that guide behavior toward the set point. Our results rule out the labeled line hypothesis, where WCs mediate warming responses and CCs mediate cooling responses. We find that warming and cooling are active in overlapping temperature ranges and each type of sensor contributes to both warming and cooling behavioral responses.

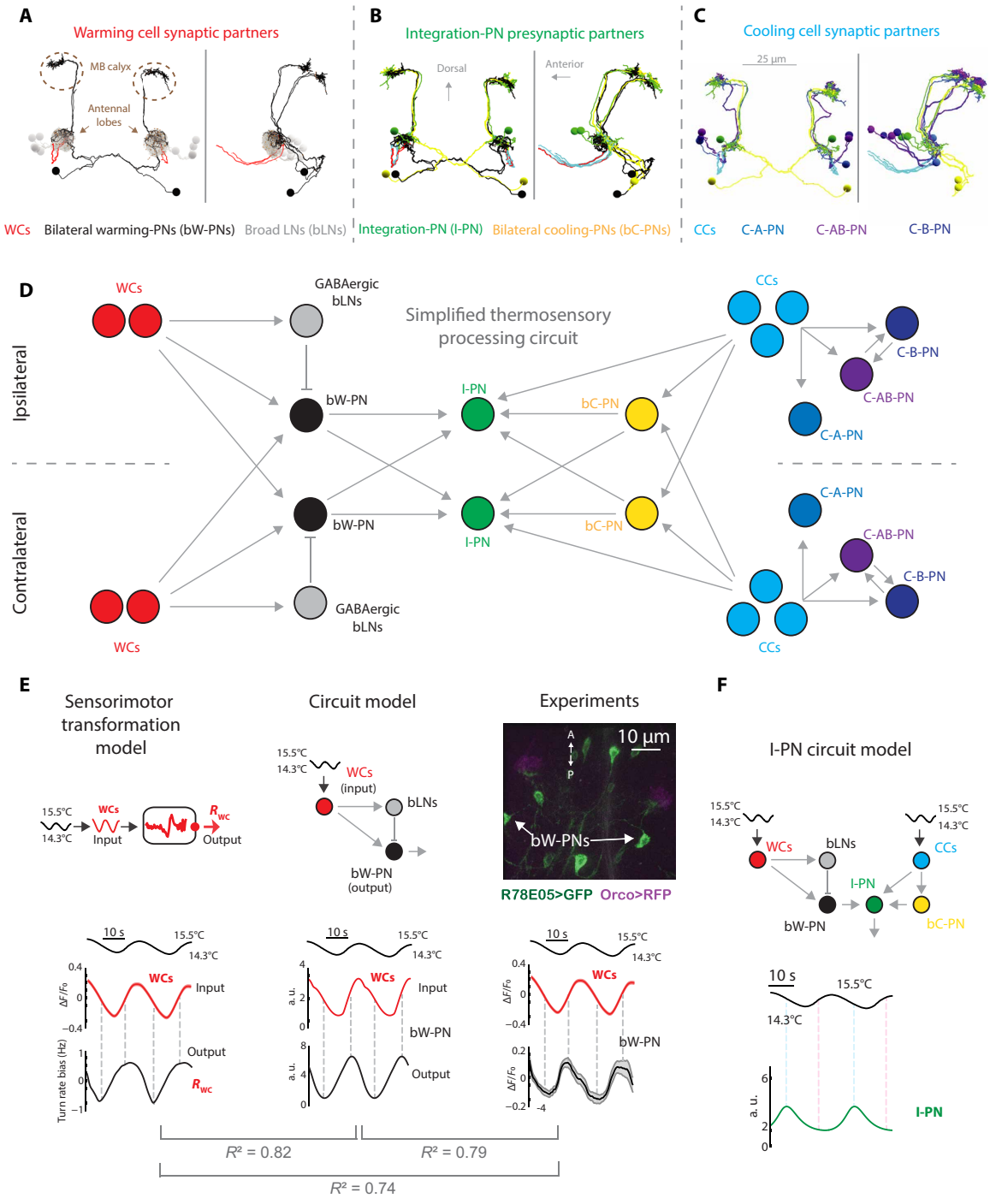

Fig. 10. Wiring diagram of second-order thermosensory circuits. (**A** to **C**) Electron microscopy reconstruction of the synaptic partners of WCs (A) and CCs (C) and presynaptic partners of the I-PN (B). MB, mushroom body. (**D**) Simplified wiring diagram of the thermosensory pathway. (**E**) Comparison between the C-IM, a circuit model, and experimental measurements in the warming pathway second-order neurons. The experimentally measured bW-PN response shows strong correlation with the internal variable R_{WC} of the C-IM model and the circuit model prediction of the bW-PN response. (**F**) Circuit model I-PN response predictions, assuming both bW-PN and bC-PN are excitatory. Shaded regions represent SEMs.

We show that flexible cross-inhibition of opponent pathways explains how the larva targets its behavioral set point and achieves homeostatic thermoregulation. We uncover anatomical and functional evidence of an early step in the computation for homeostatic thermoregulation, calculating the time derivative of WC neural activity. We also uncover connectomic evidence for direct integration of warming and cooling pathways in the larval brain. Both classes of thermosensors play important roles whether temperature is increasing

or declining in different temperature ranges, above, near, or below the set point. These roles are quantitatively described in a C-IM, providing a framework for circuit-level dissection of the behavioral mechanisms for homeostatic thermoregulation.

Encoding of thermosensory polarity by ancestral ionotropic receptors

The new set of WCs that we presented here share anatomical and genetic similarities with the CCs. Each sensor requires a distinct but partly overlapping set of ionotropic receptors to detect temperature changes. The WCs require Ir68a, Ir93a, and Ir25a to detect warming. The CCs require Ir21a, Ir93a, and Ir25a to detect cooling. The opposed thermosensitive polarity of the WCs and CCs is encoded in their heteromeric expression of sets of Ir receptors. These ionotropic receptors are conserved across insects (*41*) and have homologs in the disease vector mosquitoes *Anopheles gambiae* and *Aedes aegypti*, which use temperature cues to identify human hosts (*42*, *43*). Heat seeking by malaria vector mosquitoes relies on Ir21a-dependent receptors. Analogous to the role of Ir21a in the *Drosophila* larva, these cooling-activated mosquito receptors control behavioral responses at the elevated temperatures associated with warm-blooded prey (*43*). The combinatorial use of ionotropic receptors may be a widely used mechanism to shape the sign and sensitivity of thermosensory responses in different insects. Future structural biology studies that examine how these receptors assemble to mediate thermosensation may elucidate the transduction roles of the specific molecular receptors Ir21a and Ir68a and the co-receptors Ir93a and Ir25a.

Relevance of synchronous and opponent sensors encoding

Many sensory modalities use opponent sensors to encode environmental stimuli including photosensation, hygrosensation, and thermosensation (*6*, *21*, *37*). The larval WCs and CCs respond to temperature changes with opposite polarity but with symmetric temporal dynamics. Calcium imaging revealed that WCs and CCs share the same peak times and adaptation times to a variety of sensory stimuli. When we exposed freely moving animals to optogenetic white noise stimulation of WCs or CCs and conducted reverse-correlation analysis, we also uncovered identical transformations that convert WC and CC activity into synchronous changes in behavior. This synchrony facilitates the integration of the output of WCs and CCs by downstream circuits. In particular, synchrony makes it possible to use linear combinations of WC and CC outputs to determine behavioral responses. The use of sensors with opposed polarity has been proposed to increase the optimality of information encoding (*44*). However, the dynamic properties of sensors with opposed polarity has not been analyzed from the perspective of efficient signal processing. Our study underscores a potential advantage in signal processing of having synchronous sensors with opposed polarity. Synchrony may simplify downstream processing.

Cross-inhibition computations in biology

We found that larval *Drosophila* uses a flexible cross-inhibitory computation to achieve thermal homeostasis. Above 24. 5°C warming is unfavorable because it carries the animal further from the homeostatic set point. In this temperature range, avoidance responses during warming are strongly stimulated by WCs and moderately cross-inhibited by CCs. Below 24. 5°C, cooling is unfavorable. In this temperature range, avoidance responses during cooling are strongly stimulated by CCs and moderately cross-inhibited by WCs. Near the homeostatic set point, balanced cross-inhibition from WCs and CCs suppresses avoidance responses.

Cross-inhibition is prevalent in perceptual choice models. In these models, cross-inhibition between competing groups of neurons often enhances accuracy in decision-making. For example, in the Usher-McClelland model of primate decision-making, different neuron groups are used to represent different choices (*45*). These neurons mutually cross-inhibit their output pathways. The most strongly activated group that represents a specific choice thus biases the decisions toward one outcome by suppressing all others (*45*, *46*).

In larval *Drosophila* thermoregulation, the choice is whether to avoid cooling or warming: At high temperatures, warming should be avoided; at low temperatures, cooling should be avoided. At all temperatures, however, the CCs are always more active during cooling and the WCs are always more active during warming. Any cross-inhibition in the outputs of the WCs and CCs has to be flexible for these neurons to contribute differently to behavior in different contexts. Unlike the Usher-McClelland model, our model stipulates that flexibility is encoded in the ambient temperature–dependent weights of the WC and CC contributions to behavior and not in the WC and CC neural responses. This type of flexibility requires additional information from a sensor of absolute ambient temperature, which remains to be identified in larval *Drosophila*.

Future directions

The cross-inhibition model helped us understand how WC and CC neural dynamics are transformed into behavioral dynamics at ambient temperatures in the innocuous range (between 14° and 34°C). However, outside the innocuous temperature range, in the noxious range, the WCs and CCs also contribute to behavioral responses. We found that at ambient temperatures below 14°C, WCs contribute to cooling avoidance, and above 34°C, CCs contribute to warming avoidance (fig. S13). The change in behavioral role of the CCs might be related to the reduction in responsiveness of the B-CCs at high temperatures (Fig. 4). Examining the behavioral roles of the C-A-PNs and C-B-PNs (Fig. 10), which preferentially receive inputs from A- and B-type CCs, respectively (fig. S12), may help explain this behavioral switch.

The flexible integration of warming and cooling pathways is captured in the cross-inhibition model by the ambient temperature–dependent weights w_{WC} and w_{CC}. A neural implementation of this flexibility requires the input from an absolute ambient temperature sensor. Future studies that explore the molecular identity of this sensor may gain additional insight into the mechanisms underlying flexible warming and cooling integration.

The reconstruction of the wiring diagram of the WC and CC synaptic partners revealed that the main synaptic partners of the WCs are the bLNs (fig. S12). This connectivity pattern suggests potential thermosensory normalization of olfactory inputs, as the bLNs are the population of GABAergic interneurons that provide panglomerular inhibition to the olfactory system. Similarly, in the mushroom body connectome (*47*), the Kenyon cells that receive inputs exclusively from thermosensory pathways synapse strongly onto the GABAergic anterior paired lateral neurons, suggesting thermosensory normalization of chemosensory pathways. This anatomical evidence, coupled with the molecular access to thermosensory and olfactory receptors, makes the *Drosophila* larva an ideal model organism for the study of multisensory integration between olfactory and thermosensory pathways.

Consequences for thermal homeostasis

In mammals, prevailing models of thermoregulation propose that signals from CCs and WCs are integrated in the preoptic area of the hypothalamus (*1*). GABAergic and glutamatergic neurons are proposed to play a role in the modulation of hypothalamic WCs (*1*–*3*). However, the computations driving thermal homeostasis in mammals remain obscure and are challenging to dissect because overlapping autonomic and behavioral mechanisms contribute to thermoregulation, making the output of the computation multidimensional.

Because poikilotherms strictly use behavior for thermoregulation, measurements of behavior constitute the full output of the thermoregulatory computation. Similar to mammals, *Drosophila* integrates the outputs of bidirectional sensors of cooling and warming to regulate body temperature. The computation underlying thermal homeostasis in the larva may represent a general means of maintaining a set point using opponent sensors.

Significance for systems neuroscience

Many poikilotherms, including cave beetles (*5*) and python vipers (*48*), have neural and behavioral responses to temperature changes that are as robust as the ones displayed by larval *Drosophila*. The significance of understanding the computations underlying thermal homeostasis in *D. melanogaster* is that, unlike other poikilotherms, *Drosophila*'s genetic accessibility allows one to manipulate with precision the individual receptors and neurons underlying thermal homeostasis. In addition, the recent advances in larval *Drosophila* connectomics (*47*) and the numerical simplicity of its thermosensory system enabled us to trace the second-order warming and cooling circuits. We found a circuit that integrates inputs from bilateral warming and cooling PNs and a circuit that extracts the derivative of the WCs, both of which constitute potential implementations of components of the cross-inhibition sensorimotor transformation model (Fig. 10). However, several other undiscovered downstream circuits may implement the full sensorimotor transformation. The combination of connectome tracing and genetic identification of downstream thermosensory neurons will enable access to organism-level neural circuits underlying thermal homeostasis.

Consequences for other homeostatic control systems

Homeostatic control is pervasive in biology, including homeostatic control of synaptic plasticity in connections between neurons (*49*), homeostatic control of cardiac output (*50*), and homeostatic control of glucose (*51*). All homeostatic processes regulate a physiological variable near an optimal set point. We have identified the control system for homeostatic thermal regulation in larval *Drosophila*. We have determined the computation that integrates the outputs of WCs and CCs and established how this computation leads to control over the homeostatic variable. Our analysis establishes a framework for gaining quantitative insight into a homeostatic control system.

METHODS

Fly husbandry

Flies were raised at constant temperature (22°C) and 50% humidity on standard cornmeal agar–based medium. For experiments with larvae, adult *D. melanogaster* were transferred to collection cages (Genesee Scientific). One end of the cage held a grape juice agar plate and fresh yeast paste. Flies laid eggs on the agar plate for 2 days when the plate was removed to collect larvae. For all experiments, early second-instar larvae were selected on the basis of spiracle development using a dissection microscope.

Genotypes

The genotypes of fly stocks used in this study are as follows:

Effectors: UAS-GCaMP6m in the second chromosome: w[1118]; P[y[+t7.7] w[+mC]=20XUAS-IVS-GCaMP6m]attP40 (from BDSC 42748); UAS-GCaMP6m in the third chromosome: w[1118]; PBacy[+mDint2] w[+mC]=20XUAS-IVS-GCaMP6mVK00005 (from BDSC 42750); UAS-GFP: w[*]; P[y[+t7.7] w[+mC]=10XUAS-IVS-mCD8::GFP]attP40 (from BDSC 32186); UAS-Ir68a and UAS-Ir93a from (*26*); UAS-Ir25a from (*52*); and UAS-CsChrimson: w[1118]; Py[+t7.7] w[+mC]=20XUAS-IVS-CsChrimson.mVenusattP2 (from BDSC 55136).

Gal4-drivers: pebbled-Gal4 from (*14*), w[1118];P[Ir68a-Gal4]attp2 backcrossed from (*26*), and w[1118]; Py[+t7.7] w[+mC]=GMR11F02-GAL4attP2 from BDSC 49828.

Mutants: $Ir68a^{PB}$ from (*26*), $Ir93a^{MI05555}$ from (*21*), $Ir21a^{123}$ from (*20*), $Ir25a^{2}$ from (*28*), and Ir25a-BAC from (*2*).

Confocal microscopy

All fluorescence imaging was performed using a spinning disk confocal setup using a ×60 1.2 numerical aperture water immersion objective (Nikon Instruments LV100; Andor). During functional imaging in response to temperature changes, thermal expansion of the objective lens was compensated using a piezoelectric element (*6*). For each experiment, larvae were washed with water and partially immobilized under a coverslip (*6*). The microscope stage was temperature-controlled using a Peltier thermoelectric actuator (Custom Thermoelectric) controlled with an H-bridged power driver and a two-degrees-of-freedom Proportional, Integral, and Derivative (PID) control algorithm. This algorithm was implemented using a PID control module (Accuthermo Technologies) operated by custom code written in LabVIEW (see Extended Methods). The Peltier element was cooled by flowing antifreeze through an attached water block. The antifreeze was kept at 8° to 10°C using a VWR chiller.

Temperature-controlled behavioral apparatus

The temperature-controlled behavioral apparatus was operated inside a dark enclosure to prevent any light from causing phototactic artifacts. The behavioral arena was mounted on vibration-damping legs to eliminate mechanical artifacts. Dark-field illumination was provided with custom-built infrared light-emitting diode (LED) bars (λ, 850 nm) operated with 10% pulse width modulation to avoid heating artifacts. The behavioral arena was temperature-controlled with four Peltier thermoelectric actuators (Custom Thermoelectric) controlled with an H-bridged power driver and a two-degrees-of-freedom PID control algorithm. This algorithm was implemented with PID control modules (Accuthermo Technologies) and custom code written in LabVIEW (see Extended Methods). Feedback signals for PID control were from thermocouples located in the behavioral arena and on the agar.

During behavioral experiments, 15 to 18 larvae crawled freely for 20 min on 10 cm by 10 cm agar squares with 4-mm thickness. These surfaces contained 2% agar and 0.1% activated charcoal (Sigma-Aldrich). Charcoal increases visual contrast when imaging. We captured movies using a charge-coupled device (CCD) camera (Mightex) with a long-pass infrared filter (740 nm) at 4 frames per second (fps).

Optogenetic behavioral apparatus

For optogenetic experiments, animals were reared in cages with grape juice plates with a mixture of 0.18 g of yeast and 400 μl of 0.5 mM all-trans-retinal. The cages were kept in complete darkness until the experiment. The setup for optogenetic behavioral experiments is described elsewhere (*30*). Briefly, optogenetic light stimulation was provided by a custom-built LED matrix (SMD 5050 flexible LED strip lights; 12 V DC; λ, 625 nm). Optogenetic stimulation was controlled with an H-bridge driver and custom code written for a LabJack U3 controller. Light intensity was controlled via pulse width modulation at 500 kHz. Optogenetic stimulation was synchronized with image acquisition. Dark-field illumination was provided using custom-built infrared LED light bars (λ = 850 nm). The wavelength of infrared illumination was chosen to avoid interference with the red LED illumination for optogenetic stimulation. Infrared LEDs for dark-field illumination were mounted using optomechanical elements to adjust the angle with respect to the behavioral arena, avoiding larval "shadows" that lowered the efficiency of data acquisition. The red LEDs were connected in parallel to produce uniform illumination. We verified uniform light intensity at 1.5 W/m^2 ± 0.02. The behavioral arena was 22 cm by 22 cm and used the same agar composition as for temperature-controlled behavior experiments. In each experiment, 25 to 30 larvae were used and their movements were recorded with a CCD camera with a long-pass infrared filter (740 nm) at 4 fps. Temperature was controlled in the same way as for thermoregulation behavior experiments.

Electron microscopy of the dorsal organ ganglia

For focused ion beam scanning electron microscopy (FIB-SEM) serial sectioning, second- and third-instar wild-type Canton S larvae were used. After rinsing in phosphate-buffered saline, the anterior half of the larva was incubated in fixative [2% formaldehyde with 2.5% glutardialdehyde in 0.1 M Na-cacodylate buffer (pH 7.4); Sigma-Aldrich, Germany] for 30 to 90 min. Then, the head region was cut off and incubated in fresh fixative for 90 min. Samples were washed in Na-cacodylate, followed by postfixation in 1% osmium tetroxide (SERVA Electrophoresis GmbH, Germany) for 2 hours at 48°C in the dark. En bloc staining was carried out with 1% uranyl acetate and 1% phosphotungstic acid in 70% ethanol in the dark overnight before continuing the alcohol dehydration the next day. Samples were transferred to propylene oxide before embedded in Spurr (Plano GmbH, Germany) using ascending Spurr concentrations diluted in propylene oxide for optimal tissue infiltration. Polymerization was carried out at 65°C for 72 hours. Blocks were trimmed using an Ultracut UCT microtome (Leica, Germany), mounted on conventional SEM stubs, and sputtered with 80- to 100-nm platinum. FIB-SEM serial sectioning was carried out using a field-emission SEM Auriga CrossBeam workstation (Zeiss, Germany). FIB fine milling was carried out with 500 pA.

Electron microscopy of second-order neurons

Neurons and synapses were annotated in a complete central nervous system from a 6-hour-old [iso] Canton S G1 x w1118 larva imaged at 4.4 nm by 4.4 nm by 50 nm resolution, as described in (*33*). The full dataset of the larval *Drosophila* central nervous system is available at https://tinyurl.com/larval-cns. The wiring diagram was mapped using CATMAID (*53*), updated with the novel suite of neuron skeletonization and analysis tools (*54*).

Behavioral quantification

Behavior was preprocessed using MAGAT Analyzer (https://github.com/samuellab/MAGATAnalyzer). Every larva image was used to calculate its midline. Each midline was then segmented in 11 points. Eight behavioral parameters were calculated from the body contour and segmented midline: speed, crab speed, spine length, direction of motion, forward/backward crawling bias, head turn, head angular speed, and area of the larvae body (see Extended Methods for details). The time traces of these behavioral parameters over one period of a temperature sine wave stimulus were used to build an interpoint dissimilarity matrix, followed by multidimensional scaling, dimension selection, and an iterative denoising trees algorithm to classify larvae motor sequences in response to temperature fluctuations. This procedure was implemented following (*55*). See the details of the calculations in Extended Methods.

Sensorimotor transformation models

One component of the thermoregulatory computations is the filter that transforms the neural activity of CCs or WCs into behavioral responses. We estimated these filters by combining results from our calcium imaging experiments and optogenetic behavior experiments [see Extended Methods and (*30*)]. Briefly, the normalized measured activity responses of WCs and CCs (measured by calcium imaging) were convolved with the linear filters that convert WC and CC activities into behavioral responses (measured using optogenetics and quantitative behavioral analysis). The results of these convolutions were weighted to reflect the contribution of each sensor type to behavioral response as follows

$$R\,\mathrm{cc}_{\mathrm{turn}}(t) = \int_0^\infty H\,\mathrm{cc}_{\mathrm{turn}}(\tau)\, s_{\mathrm{CC}}(t-\tau)\, d\tau \quad (1)$$

$$R\,\mathrm{wc}_{\mathrm{turn}}(t) = \int_0^\infty H\,\mathrm{wc}_{\mathrm{turn}}(\tau)\, s_{\mathrm{WC}}(t-\tau)\, d\tau \quad (2)$$

where $H\mathrm{wc}_{\mathrm{turn}}$ and $H\mathrm{cc}_{\mathrm{turn}}$ are the convolution kernels for the WCs and CCs, respectively. Each kernel is computed from the signal history of the WCs [$s_{\mathrm{WC}}(t-\tau)$] and CCs [$s_{\mathrm{CC}}(t-\tau)$].

The turning rates calculated from Eqs. 1 and 2 are linearly combined with scalar weights, w_{CC} and w_{WC}, for all models to obtain the predicted turning rate $R_{\mathrm{turn}}(t)$ as follows

$$R_{\mathrm{turn}}(t) = w_{\mathrm{CC}} * R\,\mathrm{cc}_{\mathrm{turn}}(t) + w_{\mathrm{WC}} * R\,\mathrm{wc}_{\mathrm{turn}}(t) + \mathrm{Bl}_{\mathrm{turn}} \quad (3)$$

where $\mathrm{Bl}_{\mathrm{turn}}$ is a constant that represents the baseline turning rate of 0.05 Hz.

In the LLM, turning during cooling can only be modulated by the CCs and turning during warming can only be modulated by the WCs. These conditions amount to a rectification of the $R\mathrm{wc}_{\mathrm{turn}}$ during cooling and $R\mathrm{cc}_{\mathrm{turn}}$ during warming.

In the C-IM, turning is controlled by both WCs and CCs. The contributions of WCs and CCs ($R\mathrm{wc}_{\mathrm{turn}}$ and $R\mathrm{cc}_{\mathrm{turn}}$) to behavior are allowed to take negative values and therefore do not require a transformation to positive values or a saturation before the linear combination. Turning rates cannot be negative though, so the result of the linear combination is transformed with a linear function into non-negative values.

In the C-AM, turning is controlled by both WCs and CCs. The contributions of WCs and CCs to behavior ($R\mathrm{wc}_{\mathrm{turn}}$ and $R\mathrm{cc}_{\mathrm{turn}}$) are transformed with a linear function to have non-negative values. The

result of the linear combination will always be positive, so it does not need to be transformed again. In all cases, the values of the weights (w_{CC} and w_{WC}) are linearly regressed to match the amplitude of the wild-type animal responses.

In the updated C-IM of Fig. 7, the contributions of parallel pathways are linearly combined with the output of the WC and CC pathway. To do this, the weights w_{CC} and w_{WC} were recalculated and the turning rate responses (minus the constant baseline Bl_{turn}) of mutant larvae without functional WCs or CCs [$Pll_{turn}(t)$] were added as follows

$$R_{turn}(t) = w_{CC} * R\,cc_{turn}(t) + w_{WC} * R\,wc_{turn}(t) + Bl_{turn} + Pll_{turn}(t) \quad (4)$$

Circuit models

We used a firing rate model of the WCs, CCs, and their synaptic partners to simulate circuit function. The firing rate model can be written in vector and matrix notation with the following differential equation

$$\tau \odot \frac{dv}{dt} = -v + s + b + (v_{max} - v) \odot (M_E \cdot v) - M_I \cdot v \quad (5)$$

In Eq. 5, τ is the vector of time scales of each neuron, v is the vector of firing rates, s is the vector of external stimuli (temperature sinusoidal waves for WCs and CCs), b is the vector of baseline firing rate, v_{max} is the maximum firing rate vector, M_E is the matrix of excitatory connections, and M_I is the matrix of inhibitory connections. Also, note that $\odot$ is the operator of element-wise vector multiplication, and lowercase letters are used for vectors and capital letters are used for matrices.

The parameter v_{max} sets the maximum firing rate. Since we want to understand the system when it operates far from saturation, it is set to be 20 for all neurons; this value is high enough to avoid saturation in all the simulations that we used. The baseline firing rate is a parameter that prevents the system from reaching equilibrium at $v = 0$; it is set to be 2 to operate far from saturation. For the initial conditions of the system of differential equations, we assume that none of the thermosensory cells are active and, thus, the other network components also start inactive (at their baseline activity level). The relative time scale (τ) of PNs and local neurons in the larval thermosensory pathway was selected to approximate the average ratios in electrophysiological data of olfactory local neurons and PNs in adult *Drosophila* (*56*). For the excitatory and inhibitory matrices, synaptic weights were normalized to represent a percentage of output synapses from each neuron type. The bLNs were assigned inhibitory polarity, as they are GABAergic (*34*).

SUPPLEMENTARY MATERIAL

Supplementary material for this article is available at http://advances.sciencemag.org/cgi/content/full/7/35/eabg6707/DC1

View/request a protocol for this paper from *Bio-protocol*.

REFERENCES AND NOTES

1. J. Siemens, G. B. Kamm, Cellular populations and thermosensing mechanisms of the hypothalamic thermoregulatory center. *Pflügers Arch.* **470**, 809–822 (2018).
2. S. Hrvatin, S. Sun, O. F. Wilcox, H. Yao, A. J. Lavin-Peter, M. Cicconet, E. G. Assad, M. E. Palmer, S. Aronson, A. S. Banks, E. C. Griffith, M. E. Greenberg, Neurons that regulate mouse torpor. *Nature* **583**, 115–121 (2020).
3. T. M. Takahashi, G. A. Sunagawa, S. Soya, M. Abe, K. Sakurai, K. Ishikawa, M. Yanagisawa, H. Hama, E. Hasegawa, A. Miyawaki, K. Sakimura, M. Takahashi, T. Sakurai, A discrete neuronal circuit induces a hibernation-like state in rodents. *Nature* **583**, 109–114 (2020).
4. B. Barbagallo, P. A. Garrity, Temperature sensation in *Drosophila*. *Curr. Opin. Neurobiol.* **34**, 8–13 (2015).
5. R. Loftus, G. Corbière-Tichané, Response of antennal cold receptors of the catopid beetles, *Speophyes lucidulus* Delar. and *Cholera angustata* Fab. to very slowly changing temperature. *J. Comp. Physiol. A* **161**, 399–405 (1987).
6. M. Klein, B. Afonso, A. J. Vonner, L. Hernandez-Nunez, M. Berck, C. J. Tabone, E. A. Kane, V. A. Pieribone, M. N. Nitabach, A. Cardona, M. Zlatic, S. G. Sprecher, M. Gershow, P. A. Garrity, A. D. T. Samuel, Sensory determinants of behavioral dynamics in *Drosophila* thermotaxis. *Proc. Natl. Acad. Sci.* **112**, E220–E229 (2015).
7. M. B. Goodman, P. Sengupta, The extraordinary AFD thermosensor of *C. elegans*. *Pflügers Arch.* **470**, 839–849 (2018).
8. M. Haesemeyer, D. N. Robson, J. M. Li, A. F. Schier, F. Engert, The structure and timescales of heat perception in larval zebrafish. *Cell Syst.* **1**, 338–348 (2015).
9. H. J. Solinski, M. A. Hoon, Cells and circuits for thermosensation in mammals. *Neurosci. Lett.* **690**, 167–170 (2019).
10. L. Ni, P. Bronk, E. C. Chang, A. M. Lowell, J. O. Flam, V. C. Panzano, D. L. Theobald, L. C. Griffith, P. A. Garrity, A gustatory receptor paralogue controls rapid warmth avoidance in *Drosophila*. *Nature* **500**, 580–584 (2013).
11. J. Y. Kwon, A. Dahanukar, L. A. Weiss, J. R. Carlson, Molecular and cellular organization of the taste system in the *Drosophila* larva. *J. Neurosci.* **31**, 15300–15309 (2011).
12. J. Luo, W. L. Shen, C. Montell, Trpa1 mediates sensation of the rate of temperature change in *Drosophila* larvae. *Nat. Neurosci.* **20**, 34–41 (2017).
13. T.-W. Chen, T. J. Wardill, Y. Sun, S. R. Pulver, S. L. Renninger, A. Baohan, E. R. Schreiter, R. A. Kerr, M. B. Orger, V. Jayaraman, L. L. Looger, K. Svoboda, D. S. Kim, Ultrasensitive fluorescent proteins for imaging neuronal activity. *Nature* **499**, 295–300 (2013).
14. L. B. Sweeney, A. Couto, Y.-H. Chou, D. Berdnik, B. J. Dickson, L. Luo, T. Komiyama, Temporal target restriction of olfactory receptor neurons by semaphorin-1a/plexina-mediated axon-axon interactions. *Neuron* **53**, 185–200 (2007).
15. E. A. Pnevmatikakis, D. Soudry, Y. Gao, T. A. Machado, J. Merel, D. Pfau, T. Reardon, Y. Mu, C. Lacefield, W. Yang, M. Ahrens, R. Bruno, T. M. Jessell, D. S. Peterka, R. Yuste, L. Paninski, Simultaneous denoising, deconvolution, and demixing of calcium imaging data. *Neuron* **89**, 285–299 (2016).
16. B. L. Munger, C. Ide, The structure and function of cutaneous sensory receptors. *Arch. Histol. Cytol.* **51**, 1–34 (1988).
17. H. Wu, J. Williams, J. Nathans, Morphologic diversity of cutaneous sensory afferents revealed by genetically directed sparse labeling. *eLife* **1**, e00181 (2012).
18. R. F. Foelix, R. F. Stocker, R. A. Steinbrecht, Fine structure of a sensory organ in the arista of *Drosophila melanogaster* and some other dipterans. *Cell Tissue Res.* **258**, 277–287 (1989).
19. B. Gerber, R. F. Stocker, The *Drosophila* larva as a model for studying chemosensation and chemosensory learning: A review. *Chem. Senses* **32**, 65–89 (2007).
20. L. Ni, M. Klein, K. V. Svec, G. Budelli, E. C. Chang, A. J. Ferrer, R. Benton, A. D. Samuel, P. A. Garrity, The ionotropic receptors IR21a and IR25a mediate cool sensing in *Drosophila*. *eLife* **5**, e13254 (2016).
21. Z. A. Knecht, A. F. Silbering, L. Ni, M. Klein, G. Budelli, R. Bell, L. Abuin, A. J. Ferrer, A. D. Samuel, R. Benton, P. A. Garrity, Distinct combinations of variant ionotropic glutamate receptors mediate thermosensation and hygrosensation in *Drosophila*. *eLife* **5**, e17879 (2016).
22. G. Budelli, L. Ni, C. Berciu, L. van Giesen, Z. A. Knecht, E. C. Chang, B. Kaminski, A. F. Silbering, A. Samuel, M. Klein, R. Benton, D. Nicastro, P. A. Garrity, Ionotropic receptors specify the morphogenesis of phasic sensors controlling rapid thermal preference in *Drosophila*. *Neuron* **101**, 738–747.e3 (2019).
23. Y. Lee, S. Poudel, Y. Kim, D. Thakur, C. Montell, Calcium taste avoidance in *Drosophila*. *Neuron* **97**, 67–74.e4 (2018).
24. F. van Breugel, A. Huda, M. H. Dickinson, Distinct activity-gated pathways mediate attraction and aversion to CO_2 in *Drosophila*. *Nature* **564**, 420–424 (2018).
25. E. C. Marin, L. Büld, M. Theiss, T. Sarkissian, R. J. V. Roberts, R. Turnbull, I. F. M. Tamimi, M. W. Pleijzier, W. J. Laursen, N. Drummond, P. Schlegel, A. S. Bates, F. Li, M. Landgraf, M. Costa, D. D. Bock, P. A. Garrity, G. S. X. E. Jefferis, Connectomics analysis reveals first-, second-, and third-order thermosensory and hygrosensory neurons in the adult *Drosophila* brain. *Cell Biol.* **30**, 3167–3182.e4 (2020).
26. Z. A. Knecht, A. F. Silbering, J. Cruz, L. Yang, V. Croset, R. Benton, P. A. Garrity, Ionotropic receptor-dependent moist and dry cells control hygrosensation in *Drosophila*. *eLife* **6**, e26654 (2017).
27. J. A. Sánchez-Alcañiz, A. F. Silbering, V. Croset, G. Zappia, A. K. Sivasubramaniam, L. Abuin, S. Y. Sahai, D. Münch, K. Steck, T. O. Auer, S. Cruchet, G. L. Neagu-Maier, S. G. Sprecher, C. Ribeiro, N. Yapici, R. Benton, An expression atlas of variant ionotropic glutamate receptors identifies a molecular basis of carbonation sensing. *Nat. Commun.* **9**, 4252 (2018).
28. R. Benton, K. S. Vannice, C. Gomez-Diaz, L. B. Vosshall, Variant ionotropic glutamate receptors as chemosensory receptors in Drosophila. *Cell* **136**, 149–162 (2009).

29. L. Luo, M. Gershow, M. Rosenzweig, K. Kang, C. Fang-Yen, P. A. Garrity, A. D. T. Samuel, Navigational decision making in Drosophila thermotaxis. *J. Neurosci.* **30**, 4261–4272 (2010).
30. L. Hernandez-Nunez, J. Belina, M. Klein, G. Si, L. Claus, J. R. Carlson, A. D. Samuel, Reverse-correlation analysis of navigation dynamics in Drosophila larva using optogenetics. *eLife* **4**, e06225 (2015).
31. M. Liu, A. K. Sharma, J. W. Shaevitz, A. M. Leifer, Temporal processing and context dependency in *Caenorhabditis elegans* response to mechanosensation. *eLife* **7**, e36419 (2018).
32. N. C. Klapoetke, Y. Murata, S. S. Kim, S. R. Pulver, A. Birdsey-Benson, Y. K. Cho, T. K. Morimoto, A. S. Chuong, E. J. Carpenter, Z. Tian, J. Wang, Y. Xie, Z. Yan, Y. Zhang, B. Y. Chow, B. Surek, M. Melkonian, V. Jayaraman, M. Constantine-Paton, G. K.-S. Wong, E. S. Boyden, Independent optical excitation of distinct neural populations. *Nat. Methods* **11**, 338–346 (2014).
33. T. Ohyama, C. M. Schneider-Mizell, R. D. Fetter, J. V. Aleman, R. Franconville, M. Rivera-Alba, B. D. Mensh, K. M. Branson, J. H. Simpson, J. W. Truman, A. Cardona, M. Zlatic, A multilevel multimodal circuit enhances action selection in Drosophila. *Nature* **520**, 633–639 (2015).
34. M. E. Berck, A. Khandelwal, L. Claus, L. Hernandez-Nunez, G. Si, C. J. Tabone, F. Li, J. W. Truman, R. D. Fetter, M. Louis, A. D. Samuel, A. Cardona, The wiring diagram of a glomerular olfactory system. *eLife* **5**, e14859 (2016).
35. A. J. Kim, A. A. Lazar, Y. B. Slutskiy, Projection neurons in Drosophila antennal lobes signal the acceleration of odor concentrations. *eLife* **4**, e06651 (2015).
36. H.-H. Li, J. R. Kroll, S. M. Lennox, O. Ogundeyi, J. Jeter, G. Depasquale, J. W. Truman, A gal4 driver resource for developmental and behavioral studies on the larval cns of Drosophila. *Cell Rep.* **8**, 897–908 (2014).
37. A. Enjin, E. E. Zaharieva, D. D. Frank, S. Mansourian, G. S. B. Suh, M. Gallio, M. C. Stensmyr, Humidity sensing in Drosophila. *Curr. Biol.* **26**, 1352–1358 (2016).
38. M. Gallio, T. A. Ofstad, L. J. Macpherson, J. W. Wang, C. S. Zuker, The coding of temperature in the Drosophila brain. *Cell* **144**, 614–624 (2011).
39. A. Moqrich, S. W. Hwang, T. J. Earley, M. J. Petrus, A. N. Murray, K. S. R. Spencer, M. Andahazy, G. M. Story, A. Patapoutian, Impaired thermosensation in mice lacking trpv3, a heat and camphor sensor in the skin. *Science* **307**, 1468–1472 (2005).
40. A. Dhaka, A. N. Murray, J. Mathur, T. J. Earley, M. J. Petrus, A. Patapoutian, Trpm8 is required for cold sensation in mice. *Neuron* **54**, 371–378 (2007).
41. V. Croset, R. Rytz, S. F. Cummins, A. Budd, D. Brawand, H. Kaessmann, T. J. Gibson, R. Benton, Ancient protostome origin of chemosensory ionotropic glutamate receptors and the evolution of insect taste and olfaction. *PLOS Genet.* **6**, e1001064 (2010).
42. R. A. Corfas, L. B. Vosshall, The cation channel trpa1 tunes mosquito thermotaxis to host temperatures. *eLife* **4**, e11750 (2015).
43. C. Greppi, W. J. Laursen, G. Budelli, E. C. Chang, A. M. Daniels, L. van Giesen, A. L. Smidler, F. Catteruccia, P. A. Garrity, Mosquito heat seeking is driven by an ancestral cooling receptor. *Science* **367**, 681–684 (2020).
44. J. Gjorgjieva, M. Meister, H. Sompolinsky, Optimal sensory coding by populations of on and off neurons. bioRxiv 10.1101/131946 [**Preprint**]. 2017. https://doi.org/10.1101/131946.
45. M. Usher, J. L. McClelland, The time course of perceptual choice: The leaky, competing accumulator model. *Psychol. Rev.* **108**, 550–592 (2001).
46. T. D. Seeley, P. K. Visscher, T. Schlegel, P. M. Hogan, N. R. Franks, J. A. R. Marshall, Stop signals provide cross inhibition in collective decision-making by honeybee swarms. *Science* **335**, 108–111 (2012).
47. K. Eichler, F. Li, A. Litwin-Kumar, Y. Park, I. Andrade, C. M. Schneider-Mizell, T. Saumweber, A. Huser, C. Eschbach, B. Gerber, R. D. Fetter, J. W. Truman, C. E. Priebe, L. F. Abbott, A. S. Thum, M. Zlatic, A. Cardona, The complete connectome of a learning and memory centre in an insect brain. *Nature* **548**, 175–182 (2017).
48. E. O. Gracheva, N. T. Ingolia, Y. M. Kelly, J. F. Cordero-Morales, G. Hollopeter, A. T. Chesler, E. E. Sánchez, J. C. Perez, J. S. Weissman, D. Julius, Molecular basis of infrared detection by snakes. *Nature* **464**, 1006–1011 (2010).
49. H.-K. Lee, A. Kirkwood, Mechanisms of homeostatic synaptic plasticity in vivo. *Front. Cell. Neurosci.* **13**, 520 (2019).
50. W. E. Whitehead, V. M. Drescher, P. Heiman, B. Blackwell, Relation of heart rate control to heartbeat perception. *Biofeedback Self Regul.* **2**, 371–392 (1977).
51. E. D. Rosen, B. M. Spiegelman, Adipocytes as regulators of energy balance and glucose homeostasis. *Nature* **444**, 847–853 (2006).
52. L. Abuin, B. Bargeton, M. H. Ulbrich, E. Y. Isacoff, S. Kellenberger, R. Benton, Functional architecture of olfactory ionotropic glutamate receptors. *Neuron* **69**, 44–60 (2011).
53. S. Saalfeld, B. Bargeton, M. H. Ulbrich, E. Y. Isacoff, S. Kellenberger, R. Benton, Catmaid: Collaborative annotation toolkit for massive amounts of image data. *Bioinformatics* **25**, 1984–1986 (2009).
54. C. M. Schneider-Mizell, S. Gerhard, M. Longair, T. Kazimiers, F. Li, M. F. Zwart, A. Champion, F. M. Midgley, R. D. Fetter, S. Saalfeld, A. Cardona, Quantitative neuroanatomy for connectomics in Drosophila. *eLife* **5**, e12059 (2016).
55. J. T. Vogelstein, Y. Park, T. Ohyama, R. A. Kerr, J. W. Truman, C. E. Priebe, M. Zlatic, Discovery of brainwide neural-behavioral maps via multiscale unsupervised structure learning. *Science* **344**, 386–392 (2014).
56. R. I. Wilson, G. C. Turner, G. Laurent, Transformation of olfactory representations in the Drosophila antennal lobe. *Science* **303**, 366–370 (2004).
57. K. Song, H. Wang, G. B. Kamm, J. Pohle, F. de Castro Reis, P. Heppenstall, H. Wende, J. Siemens, The trpm2 channel is a hypothalamic heat sensor that limits fever and can drive hypothermia. *Science* **353**, 1393–1398 (2016).
58. R. J. Schepers, M. Ringkamp, Thermoreceptors and thermosensitive afferents. *Neurosci. Biobehav. Rev.* **34**, 177–184 (2010).
59. W. Li, S. H. DeVries, Bipolar cell pathways for color and luminance vision in a dichromatic mammalian retina. *Nat. Neurosci.* **9**, 669–675 (2006).
60. E. V. Famiglietti Jr., A. Kaneko, M. Tachibana, Neuronal architecture of on and off pathways to ganglion cells in carp retina. *Science* **198**, 1267–1269 (1977).
61. W. W. Liu, O. Mazor, R. I. Wilson, Thermosensory processing in the Drosophila brain. *Nature* **519**, 353–357 (2015).
62. D. D. Frank, G. C. Jouandet, P. J. Kearney, L. J. Macpherson, M. Gallio, Temperature representation in the Drosophila brain. *Nature* **519**, 358–361 (2015).
63. L. Van Giesen, L. Hernandez-Nunez, S. Delasoie-Baranek, M. Colombo, P. Renaud, R. Bruggmann, R. Benton, A. D. T. Samuel, S. G. Sprecher, Multimodal stimulus coding by a gustatory sensory neuron in Drosophila larvae. *Nat. Commun.* **7**, 10687 (2016).
64. H. Altner, R. Loftus, Ultrastructure and function of insect thermo-and hygroreceptors. *Annu. Rev. Entomol.* **30**, 273–295 (1985).
65. F. Ding, Y. Shi, T. Chen, Gradient-based identification methods for hammerstein nonlinear armax models. *Nonlin. Dynam.* **45**, 31–43 (2006).
66. M. Araki, H. Taguchi, Two-degree-of-freedom pid controllers. *Int. J. Control Autom. Syst.* **1**, 401–411 (2003).
67. J. S. Bell, R. I. Wilson, Behavior reveals selective summation and max pooling among olfactory processing channels. *Neuron* **91**, 425–438 (2016).
68. M. Gershow, M. Berck, D. Mathew, L. Luo, E. A. Kane, J. R. Carlson, A. D. T. Samuel, Controlling airborne cues to study small animal navigation. *Nat. Methods* **9**, 290–296 (2012).
69. S. A. M. Ebrahim, H. K. M. Dweck, J. Stökl, J. E. Hofferberth, F. Trona, K. Weniger, J. Rybak, Y. Seki, M. C. Stensmyr, S. Sachse, B. S. Hansson, M. Knaden, Drosophila avoids parasitoids by sensing their semiochemicals via a dedicated olfactory circuit. *PLOS Biol.* **13**, e1002318 (2015).

Acknowledgments: We acknowledge members of the Samuel and Garrity laboratories for helpful discussions and comments on the manuscript. We thank R. Wilson, S. R. Datta, and A. Schier for helpful discussions and advice during the development of the project. We thank K. Vogt for helping us identify the line R78E05-Gal4 in FlyLight. We acknowledge the Bloomington Drosophila Stock Center (NIH P40OD018537). **Funding:** L.H.-N., G.B., P.G., and A.D.T.S. were supported by the NIH R01 GM130842-01 grant. A.S.T., V.R., and A.R. were supported by the Deutsche Forschungsgemeinschaft (TH1584/3-1, TH1584/6-1, and TH1584/7-1). G.B. and P.G. were also supported by NSF IOS-1557781. **Author contributions:** L.H.-N., P.G., and A.D.T.S. designed the study, interpreted the results, and wrote the manuscript with feedback from all authors. L.H.-N. developed the experimental techniques; wrote the software for data analysis; analyzed data; performed behavioral, functional imaging, and optogenetic experiments; and built the sensorimotor models and the circuit models. A. Ch. performed behavior, functional imaging, and optogenetic experiments. G.B. conducted immunostaining and light microscopy anatomy experiments. M.E.B. and A. Ca. traced the synaptic connections of the thermosensory circuits. V.R., A.R., and A.S.T. contributed the electron microscopy dataset of the dorsal organ ganglia. M.K. provided reagents, preliminary data, and technical advice. **Competing interests:** The authors declare that they have no competing interests. **Data and materials availability:** The data, code, and methods needed to evaluate the conclusions in the paper are present in the paper, in the Supplementary Materials, and in the GitHub page of this manuscript (https://github.com/LuisM6/ThermotaxisCrossInhibition2021). Genetic reagents are available upon request to the corresponding authors.

Submitted 21 January 2021
Accepted 9 July 2021
Published 27 August 2021
10.1126/sciadv.abg6707

Citation: L. Hernandez-Nunez, A. Chen, G. Budelli, M. E. Berck, V. Richter, A. Rist, A. S. Thum, A. Cardona, M. Klein, P. Garrity, A. D. T. Samuel, Synchronous and opponent thermosensors use flexible cross-inhibition to orchestrate thermal homeostasis. *Sci. Adv.* **7**, eabg6707 (2021).